

© 2022 IEEE. Personal use of this material is permitted. Permission from IEEE must be obtained for all other uses, including reprinting/republishing this material for advertising or promotional purposes, collecting new collected works for resale or redistribution to servers or lists, or reuse of any copyrighted component of this work in other works. This work has been submitted to the IEEE for possible publication. Copyright may be transferred without notice, after which this version may no longer be accessible.

arXiv:2312.06304v1 [cs.LG] 11 Dec 2023

Orchestrated Robust Controller for the Precision Control of Heavy-duty Hydraulic Manipulators

Mahdi Hejrati , Jouni Mattila 

Abstract—Vast industrial investment along with increased academic research on hydraulic heavy-duty manipulators has unavoidably paved the way for their automatization, necessitating the design of robust and high-precision controllers. In this study, an orchestrated robust controller is designed to address the mentioned issue. To do so, the entire robotic system is decomposed into subsystems, and a robust controller is designed at each local subsystem by considering unknown model uncertainties, unknown disturbances, and compound input constraints, thanks to virtual decomposition control (VDC). As such, radial basic function neural networks (RBFNNs) are incorporated into VDC to tackle unknown disturbances and uncertainties, resulting in novel decentralized RBFNNs. All these robust local controllers designed at each local subsystem are, then, orchestrated to accomplish high-precision control. In the end, for the first time in the context of VDC, a semi-globally uniformly ultimate boundedness is achieved under the designed controller. The validity of the theoretical results is verified by performing extensive simulations and experiments on a 6-degrees-of-freedom industrial manipulator with a nominal lifting capacity of 600 kg at 5 meters reach. Comparing the simulation result to state-of-the-art controller along with provided experimental results, demonstrates that the proposed method established all the promises and performed excellently.

I. INTRODUCTION

A. Heavy-duty Hydraulic Manipulators

BECAUSE of their higher robustness and remarkably larger payload-to-weight ratio (PWR), heavy-duty hydraulic manipulators (HHMs) have been widely utilized in various fields, including construction, forestry, and agriculture. For example, the commercial manipulator shown in Fig. 1 has a lifting capacity of 600 kg at 5 meters reach, with a total weight of 445 kg (PWR almost 1:1), whereas the ABB robot [1] has a lifting capacity of 550 kg at 4.2 meters with the robot weight of 4,600 kg (PWR of 1:8). Such structural rigidity of the electrical manipulators is important to achieve higher accuracy in the manufacturing industry, while in the field robotic applications, lightweight HHMs are particularly suited for installation on mobile machines, addressing the critical requirement for traversability. Consequently, it has become crucial to design a high-precision controller for HHMs that preserves their superior traversability feature while attaining the precision of electrical manipulators. The current vast

amount of industrial investments with increased academic interests will revolutionize the HHM industry [2]–[5].

Despite their advantages, HHMs suffer from fundamental challenges, such as model nonlinearities and complexities emerging from structural complicatedness and fluid dynamics [5]. In contrast to electric actuators, whose model complexity can be neglected, hydraulic actuators are governed by fluid dynamics and may be subjected to nonsmooth and discontinuous nonlinearities due to friction between cylinder and piston, compound input constraints, and valve under/overlap. Opposite to the electrically actuated open-chain manipulators, HHMs mostly comprise parallel-serial structures [6] that convert linear piston motion to rotational motion. Meanwhile, in rotary hydraulic actuators, the helical gears are employed to convert the piston motion to rotation, the same mechanism in the wrist actuators of the manipulator in this study (Fig. 1), one of which can deliver $2,000 N \cdot m$ of torque. The mentioned nonlinearities and complexities render the stability analysis and control design of HHMs significantly challenging, emphasizing the need for robust and high-performance control schemes, not only in theory but also in real-world applications.

B. State-of-the-Art Review

As explained above, HHMs are characterized by a variety of nonlinearities. Therefore, a nonlinear model-based controller (NMBC) can obtain a better performance than linear controllers [7]. In [8], different NMBC methods, such as sliding mode control (SMC), adaptive inverse dynamics controller (AIDC), and model-reference adaptive controllers with velocity measurement (MRACV), have been designed and compared, unveiling the better performance of MRACV in comparison to AIDC and SMC. In [9], an observer-based adaptive robust controller (ARC) has been designed to control a hydraulic manipulator, in which the backstepping approach has been employed to derive the control law. However, the experimental results in [10] with desired compensation ARC (DCARC) have shown that DCARC yields lower tracking error than ARC. Further, in [11] an adaptive output force tracking controller has been designed to control a 6-degrees-of-freedom (DoF) hydraulic manipulator by employing the virtual decomposition control (VDC) scheme, which was first introduced in [12]. A VDC control, also, in [13] has been designed for the precision control of a hydraulic crane. Additionally, in [14], a VDC-based separate meter-in separate meter-out controller has been presented to not only control the 3-DoF HHM but also improve the energy efficiency of the hydraulic actuator, resulting in a 47% reduction in energy

This work is supported by Business Finland partnership project "Future all-electric rough terrain autonomous mobile manipulators" (Grant 2334/31/222).

M. Hejrati, corresponding author, is with the Department of Engineering and Natural Science, Tampere University, 7320 Tampere, Finland (e-mail: mahdi.hejrati@tuni.fi).

J. Mattila is with the Department of Engineering and Natural Science, Tampere University, 7320 Tampere, Finland (e-mail: jouni.mattila@tuni.fi).

consumption. Moreover, in [15], an adaptive controller with gravity and friction identification has been developed for n-link hydraulic manipulators, and experimental results have been performed for 5-DoF HHM. In [16], a neural adaptive dynamic surface method has been proposed to control the n-link hydraulic manipulator, similar to the traditional backstepping method. The asymptotic convergence of errors with semiglobal boundedness has been proved for the system in the presence of model uncertainty and disturbance. Moreover, the combination of the time delay control with terminal SMC has been utilized to address the control problems of excavators in [17]. A prescribed performance-based adaptive neural controller has been designed in [18] to achieve a good performance for HHM. In both [16] and [18] the radial basic function neural networks (RBFNNs) are employed to estimate uncertainties.

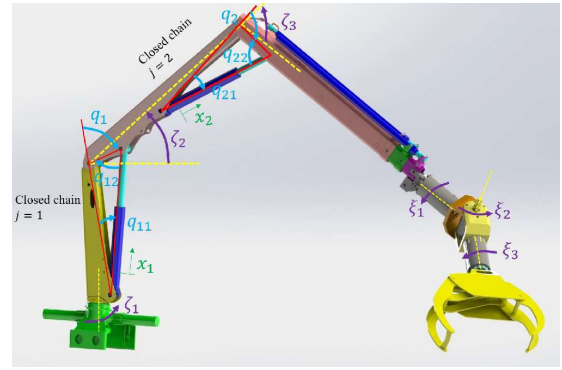
Based on [5], an appropriate way of evaluating and comparing the proposed methods in the field of HHMs is using the following performance index [11]:

$$\rho = \frac{|e|_{max}}{|\dot{x}|_{max}} \quad (1)$$

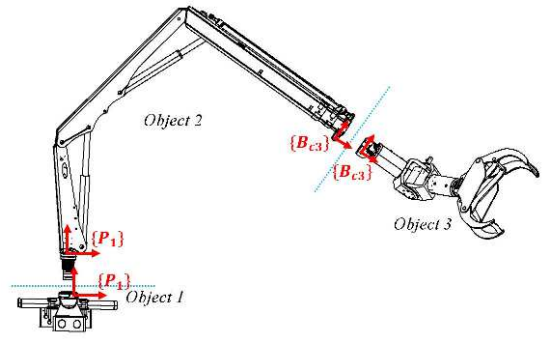
with $|e|_{max}$ and $|\dot{x}|_{max}$ denoting the absolute value of the maximum tracking error and velocity, respectively. A smaller value of ρ demonstrates a better performance for the controller. The ρ value for the controllers in [8], [10], [11], [13], [17], and [14] are 0.0044, 0.005, 0.005, 0.0039, 0.058, and 0.003, respectively. Thus, such a comparison demonstrates that the VDC approach has shown significant performance in comparison to DCARC, SMC, TSMC, and backstepping.

In addition to its better performance, the VDC scheme as a baseline controller offers other benefits, as follows: 1) It decomposes the entire complex system into subsystems where the decentralized controller and stability analysis can be performed; 2) the dynamics of each subsystem remains relatively simple, with fixed dynamic structures invariant to the target system; and 3) all uncertainties can be addressed at local subsystems. Moreover, the VDC controller designed for the electric manipulator can be applied to the hydraulic manipulator by only changing the subsystem related to the actuator while the rigid body part remains the same [12]. This is unlike other methods, in which applying a controller designed for electric robots to hydraulic robots requires redesigning the entire control scheme. Additionally, VDC has displayed a great performance in various fields, such as bilateral teleoperation [19], impedance control [20], and physical human-robot interaction [21]. All the mentioned benefits of VDC express the motivation of this paper to employ it as a baseline controller in this study.

Despite all its benefits, VDC suffers from some drawbacks as well. As expressed in [18] and [16], strong stability in the presence of model uncertainty and disturbance for hydraulic manipulators is both critical and in high demand. However, VDC ensures the L_2 boundedness for the states of the system which is not strong in the presence of uncertainties, especially when there is compound input constraint, such as deadzone in servo valves and backlash in the gears. Consequently, to have a robust VDC, it is essential to consider unknown model uncertainty, unknown disturbance, and input constraints in



(a)



(b)

Fig. 1. a) Heavy-duty hydraulic manipulator schematic with kinematic detail, b) Decomposition of the robot into objects: object 1 contains a base joint with hydraulic rack and pinion mechanism, object 2 includes two parallel mechanisms, and object 3 encompasses a spherical hydraulic wrist.

the control design while ensuring strong boundedness and stability. These are the open problems in the context of the VDC scheme. Since VDC has shown a better performance than other controllers in the field of HHM, and there is a high demand for HHM in the industry, having a robust VDC would be significantly helpful for paving the way for industrial growth. The contributions of this study properly address the mentioned issues of the VDC.

Due to their universality and perfect capabilities in function approximation, RBFNNs are widely used in robotics and control applications to estimate model uncertainty and disturbances [22], [23]. In [16], [18], [24], uncertainties of hydraulic actuators are estimated using RBFNNs, and uniformly ultimate boundedness (UUB) is proved with asymptotic tracking of the desired trajectory, highlighting the importance of achieving UUB in the presence of uncertainties. In the mentioned works, RBFNN is used to estimate disturbances and uncertainties in a rigid body-actuator model, while separately performing the estimations in actuator and rigid body parts will increase the accuracy. This is especially important in HHMs where the governing dynamics of the actuator and rigid body are completely different (the actuator is governed by fluid dynamics), and separate RBFNNs with corresponding input should be designed to learn the nature of the subsystem. It is stated in [25] that learning for complex systems (like uncertainty and disturbance estimation in 6-DoF HHM) should be solved using the decomposition and re-composition methods. This approach

is adopted in our paper for the first time by incorporating RBFNNs into VDC. Decomposing the entire model into subsystems, VDC enables us to design RBFNNs for each subsystem based on the states of that subsystem, like required spatial velocity and acceleration in rigid body subsystems and pressure and piston position and velocity in the actuator subsystem. Then, by orchestrating RBFNNs at the subsystem levels, the re-composed form of estimation is achieved for the complex model. Consequently, the incorporation of RBFNNs into VDC results in novel decentralized RBFNNs (DRBFNNs), feeding which, with the corresponding inputs of a subsystem, will increase the accuracy of the estimation. Such a novel incorporation, despite its mathematical challenges in stability analysis, is important in the sense of performance improvement.

By incorporating input constraints, control systems can operate reliably and prevent undesirable outcomes by respecting the physical limitations of the controlled system or device. The adaptive backlash inverse method introduced in [26] and the adaptive deadzone inverse method introduced in [27] are widely utilized to tackle unknown backlash or deadzone in electric robots [28], [29]. However, a limited amount of research has been conducted to address input constraint in the field of hydraulic manipulators [30]–[32]. As stated in [30], backlash and deadzone existing in the valve and gears can result in performance deterioration and even instability. In [33] and [34], the backlash in hydraulic rotary actuators with both rack and pinion mechanism and helical gear has been examined, and a better performance in experiments has been achieved. However, none of the studies considered both backlash and deadzone as compound input constraints in their control method, which is especially crucial for hydraulic actuators because they are more prone to such a compound constraint. In [35], a compound constraint consisting of saturation and backlash/deadzone is converted to an equivalent saturation function using the right inverse of the backlash or deadzone function. However, in real-world applications, the actual parameter of the backlash or deadzone is unavailable, and such an inverse cannot be computed. In this study, the compound input constraint is considered in the control design. The parametrizable part of the deadzone-backlash function is tackled by adaptive control, while the non-parametrizable part is estimated by DRBFNNs to ensure robustness.

C. Contributions

In this study, compound input constraint, unknown model uncertainty, and unknown disturbance are considered in the VDC scheme to ensure the robustness and perfect performance of the controller. Altogether, this has given rise to the orchestrated robust controller: orchestrating all the local controllers at the rigid body and actuator subsystems that are equipped to achieve high-precision control. As such, the contributions of this study can be stated with their significance as follows:

- The compound input constraint model is considered in the modeling part and handled by designing a novel adaptive deadzone-backlash inverse controller. The parametrizable part of the deadzone-backlash model is used to handle parameter uncertainties while the non-parametrizable

part, which contains all the nonlinearities, is tackled by novel DRBFNNs. In addition, DRBFNNs are employed to estimate unknown model uncertainties and unknown disturbances in actuator and rigid body subsystems.

- Taking the presented orchestrated robust controller into account along with the complexity of the system, semi-global uniformly ultimate boundedness (SGUUB) is achieved for the first time for VDC. This is a significant contribution, since achieving such stability is mathematically challenging because of the existence of VPFs and the fact that VDC deals with each subsystem.
- The results are experimentally validated using a 6-DoF commercial hydraulic manipulator, shown in Fig. 1. This is another significance of the presented paper. Although in [16], [18] neural adaptive controllers are designed for hydraulic manipulators, only simulation results of a 2-DoF robot were provided.

The rest of the paper is organized as follows. Section II expresses the fundamental mathematics of the VDC approach along with the essential lemmas and definitions utilized in this paper. Section III describes the modeling of the rigid body subsystem, whereas in Section IV, the details of the proposed controller are expressed. The low-level control design procedure for the hydraulic actuator is provided in Section V. The stability of the entire system under the proposed approach is proved in Section VI. The experimental and simulation results are provided in Section VII, and the validity of the stability and control results are verified. Finally, Section VIII concludes this study.

II. MATHEMATICAL PRELIMINARIES

In this section, the basic mathematical foundation of the VDC approach is presented, which is essential for control design and stability analysis. Moreover, lemmas and assumptions that are employed in the paper for stability analysis are expressed in this section as well. Fig. 1 demonstrates the schematics of the hydraulic robotic system in this study. Fig. 1a shows the kinematic details with base angle (ζ_1), lift angle (ζ_2), tilt angle (ζ_3), and spherical wrist angles of (ξ_1), (ξ_2), and (ξ_3). Further, Fig. 1b displays the system that decomposed into three objects, each of which will be analyzed separately, by exploiting the virtual cutting point (VCP) concept of VDC.

A. VDC Foundation

In the VDC context, linear/angular velocities and forces/moments are properly integrated within a 6D vector to facilitate the transformation of velocities and forces/moments between different frames. Spatial 6D vectors, which are based on Plücker coordinates, allow the complete representation of both linear and angular motion of multibody mechanisms in a compact manner.

Consider $\{A\}$ and $\{B\}$ as frames that are attached to the i^{th} rigid body. Then, the 6D linear/angular velocity vector ${}^A V \in \mathbb{R}^6$ and force/moment vector ${}^A F \in \mathbb{R}^6$ can be expressed as follows [12]:

$${}^A V = [{}^A v, {}^A \omega]^T, \quad {}^A F = [{}^A f, {}^A m]^T$$

where ${}^A v \in \mathbb{R}^3$ and ${}^A \omega \in \mathbb{R}^3$ are the linear and angular velocities of frame $\{A\}$, and ${}^A f \in \mathbb{R}^3$ and ${}^A m \in \mathbb{R}^3$ are the force and moment expressed in frame $\{A\}$, respectively. The transformation matrix that transforms force/moment vectors and velocity vectors between frames $\{A\}$ and $\{B\}$ is [12],

$${}^A U_B = \begin{bmatrix} {}^A R_B & \mathbf{0}_{3 \times 3} \\ ({}^A r_{AB \times}) {}^A R_B & {}^A R_B \end{bmatrix} \quad (2)$$

where ${}^A R_B \in \mathbb{R}^{3 \times 3}$ is a rotation matrix between frame $\{A\}$ and $\{B\}$, and $({}^A r_{AB \times})$ is a skew-symmetric matrix operator defined in [12]. Based on (2), the force/moment and velocity vectors can be transformed between frames as [12],

$${}^B V = {}^A U_B^T {}^A V, \quad {}^A F = {}^A U_B {}^B F. \quad (3)$$

The net force/moment vector of the rigid body in frame $\{A\}$, indicated as ${}^A F^* \in \mathbb{R}^6$, is:

$$M_A \frac{d}{dt} ({}^A V) + C_A ({}^A \omega) {}^A V + G_A = {}^A F^* \quad (4)$$

where $M_A \in \mathbb{R}^{6 \times 6}$ is the mass matrix, $C_A ({}^A \omega) \in \mathbb{R}^{6 \times 6}$ is the matrix of Coriolis and centrifugal terms and $G_A \in \mathbb{R}^6$ includes the gravity terms. Details are expressed in [36].

Property 1: [36]. The equation (4) can be written in linear-in-parameter form as below,

$$M_A \frac{d}{dt} ({}^A V) + C_A ({}^A \omega) {}^A V + G_A = \bar{Y}_A \phi_A \quad (5)$$

with $\bar{Y}_A \in \mathbb{R}^{6 \times 10}$ is the compact regressor matrix and $\phi_A \in \mathbb{R}^{10}$ is the unique inertial parameter vector.

The design variable in the VDC approach is the required velocity that can be designed for either motion control [36] or compliance control [21]. As this study examines only the free motion task, the required joint velocity is defined as:

$$\dot{p}_r = \dot{p}_d + \lambda (p_d - p). \quad (6)$$

with \dot{p}_d being desired joint velocity, p_d being desired joint trajectory, p being measured joint variable, and $\lambda > 0$ being a positive constant. The variable p depends on the type of joint; if the joint is revolute, p represents angular measurements, and if the joint is prismatic, p denotes linear motion. Then, the linear/angular velocity vector, indicated as ${}^A V_r$, can be computed based on \dot{p}_r by performing kinematic computation, for which the thorough details will be provided later. Thus, the required force/moment vector can be defined as:

$${}^A F_r^* = Y_A \hat{\phi}_A + {}^A F_c. \quad (7)$$

where Y_A is in the sense of (5) by replacing ${}^A V$ with ${}^A V_r$, $\hat{\phi}_A$ is the estimation of ϕ_A , and ${}^A F_c$ is the regulating control term. The required force/moment vector in (7) demonstrates the amount of force/moment that must be applied to the rigid body subsystem in order to achieve the control objectives at the subsystem level. In the context of VDC, each subsystem (rigid body and actuator) has a corresponding local required control action that accomplishes the local control goals. Then, by orchestrating all these local controllers, the primary goal of the system can be established. Such decomposition into subsystems and orchestration to achieve objectives are due to the VCP and VPF properties of the VDC.

Definition 1: [12]. A VCP is a directed separation interface that conceptually cuts through a rigid body. At the cutting point, the two parts resulting from the virtual cut maintain an equal position and orientation.

Definition 2: [12]. Given the frame $\{A\}$, the VPF can be defined as,

$$p_A = ({}^A V_r - {}^A V)^T ({}^A F_r - {}^A F).$$

Definition 3: [12]. A non-negative accompanying function $\nu(t) \in R$ is a piecewise differentiable function that encompasses the following properties: i) $\nu(t) \leq 0$ for $t > 0$, and ii) $\dot{\nu}(t)$ exists almost everywhere.

Definition 4: The following unit vectors are used in the VDC context: $x_f = (1, 0, 0, 0, 0, 0)^T$, $y_f = (0, 1, 0, 0, 0, 0)^T$, $z_f = (0, 0, 1, 0, 0, 0)^T$, $x_\tau = (0, 0, 0, 1, 0, 0)^T$, $y_\tau = (0, 0, 0, 0, 1, 0)^T$, $z_\tau = (0, 0, 0, 0, 0, 1)^T$.

B. Lemmas and Assumptions

In this section, we comprehensively enumerate and expound upon all the lemmas and assumptions that serve as foundational elements within the context of this paper.

Assumption 1: For an unknown external disturbance $D(t)$ and unknown robot model uncertainties Δ_R and Δ_a corresponding to rigid body and actuator subsystems, respectively, we have,

$$|D(t)| \leq \delta_1, \quad |\Delta_R| \leq \delta_2, \quad |\Delta_a| \leq \delta_3,$$

with $\delta_1, \delta_2, \delta_3 \geq 0$ being unknown constants.

Assumption 2: Because only the friction between the piston and cylinder in hydraulic actuators is critical, friction moments in all the rotating joints are equal to zero.

Lemma 1: [37]. RBFNNs can be utilized to estimate an unknown continuous function $Z(\chi) : \mathbb{R}^m \rightarrow \mathbb{R}$ with the approximation of,

$$Z(\chi) = \hat{W}^T \Psi(\chi) + \hat{\varepsilon}$$

where $\chi = [\chi_1, \chi_2, \dots, \chi_m]^T \in \mathbb{R}^m$ is the input vector of the neural networks, \hat{W} is the weight vector of the neural networks, $\Psi(\chi)$ is the basis function of the RBFNNs, and $\hat{\varepsilon}$ is the approximation error. The optimal weight vector W^* can be expressed by,

$$W^* = \arg \min_{\hat{W} \in \Xi_N} \left\{ \sup_{\chi \in \Xi_T} |\hat{Z}(\chi|\hat{W}) - Z(\chi)| \right\}$$

where $\Xi_N = \{\hat{W} \mid \|\hat{W}\| \leq \kappa\}$ is a valid set of vectors with κ being a design value, Ξ_T is an allowable set of the state vectors, and $\hat{Z}(\chi|\hat{W}) = \hat{W}^T \Psi(\chi)$.

Lemma 2: [36], [38]. For any inertial parameter vector ϕ_A , there is a one-to-one linear map $f : \mathbb{R}^{10} \rightarrow S(4)$ such that,

$$f(\phi_A) = \mathcal{L}_A = \begin{bmatrix} 0.5 \text{tr}(\bar{I}) \cdot \mathbf{1} - \bar{I} & h \\ h^T & m \end{bmatrix}$$

$$f^{-1}(\phi_A) = \phi_A(m, h, \text{tr}(\Sigma)) \cdot \mathbf{1} - \Sigma$$

where $\Sigma = 0.5 \text{tr}(\bar{I}) - \bar{I}$, and m, h , and \bar{I} are the mass, first mass moment, and rotational inertia matrix, respectively, with

$\phi_A = [m, h, \text{vec}I]$ where $\text{vec}I = [\bar{I}_{xx}, \bar{I}_{yy}, \bar{I}_{zz}, \bar{I}_{xy}, \bar{I}_{yz}, \bar{I}_{xz}]$. Moreover, $\text{tr}(\cdot)$ is the Trace operator of a matrix.

Lemma 3: [38]. For \mathcal{L}_A defined in Lemma (2), Bregman divergence with the log-det function can be defined as,

$$\mathcal{D}_F(\mathcal{L}_A \parallel \hat{\mathcal{L}}_A) = \log \frac{|\hat{\mathcal{L}}_A|}{|\mathcal{L}_A|} + \text{tr}(\hat{\mathcal{L}}_A^{-1} \mathcal{L}_A) - 4.$$

with the time derivative of,

$$\dot{\mathcal{D}}_F(\mathcal{L}_A \parallel \hat{\mathcal{L}}_A) = \text{tr}([\hat{\mathcal{L}}_A^{-1} \dot{\hat{\mathcal{L}}}_A \hat{\mathcal{L}}_A^{-1}] \tilde{\mathcal{L}}_A)$$

where $\tilde{\mathcal{L}}_A = \hat{\mathcal{L}}_A - \mathcal{L}_A$. The Bregman divergence denotes the distance between the actual value \mathcal{L}_A and its estimation $\hat{\mathcal{L}}_A$ over the manifold $\mathcal{M} \simeq \{\mathcal{L}_A \in \mathcal{S}(4) : \mathcal{L}_A \succ 0\} = \mathcal{P}(4)$, with $\mathcal{S}(4)$ being space of 4×4 real-symmetric matrices and $\mathcal{P}(4)$ being space of 4×4 real-symmetric, positive-definite matrices.

III. MODELING THE RIGID BODY SUBSYSTEM

In this section, equations of motion for the 6-DoF HHM are derived. Since VDC is an NE-based approach, it is required to perform forward velocity computation and force backpropagation to achieve dynamic equations. As demonstrated in Fig. 1b, the entire complex system is divided into three objects, which are analyzed separately. Such a decomposition may help ease the understanding of the modeling and control design, as the HHM in this study is a complex system consisting of a rack and pinion joint, serial-parallel joints, and hydraulic rotary joints. By employing VDC, each subsystem, representing a rigid body or actuator, is treated individually.

A. Kinematics of the Manipulator

In this part, kinematic analyses are performed separately for each object, representing a critical step in the VDC context that paves the way to compute total forces applied to rigid bodies.

1) *Kinematics of Object 1:* Consider ${}^G V$ to be the linear/angular velocity vector of the ground. The pillar velocity ${}^{P_1} V$ can be computed according to Fig. 2:

$${}^{P_1} V = {}^G U_{P_1}^T {}^G V + y_\tau \dot{\zeta}_1 \quad (8)$$

with ${}^G U_{P_1}$ being in the sense of (2). In (8), the $\dot{\zeta}_1$ is the angular velocity of the pillar that can be computed by numerically differentiating the encoder angle data. This angular motion is generated by the piston's linear motion through the rack and pinion mechanism. For a more accurate analysis, the dynamics of the piston must be considered as well. According to Fig. 2, we have:

$${}^{P_{p2}} V = {}^{P_{p1}} U_{P_{p2}}^T {}^{P_{p1}} V + x_f \dot{x}_p \quad (9)$$

with \dot{x}_p being the linear velocity of the piston. The following relation between the angular velocity of the pillar and the linear velocity of the piston holds:

$$\dot{x}_p = r_p \dot{\zeta}_1 \quad (10)$$

with r_p being the radius of the pinion in Fig. 2.

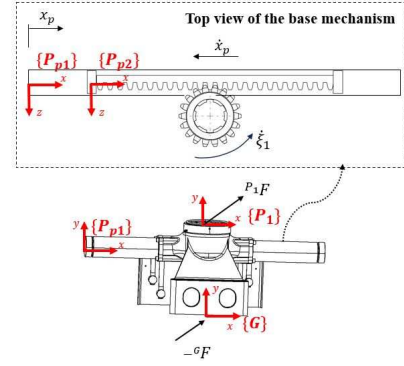


Fig. 2. VDC frames of object 1

2) *Kinematics of Object 2:* As demonstrated in Fig. 1b, object 2 is composed of two closed-chain kinematics, each of which has important geometric relations that represent constraints in the chain. In the following, the mentioned geometric relations are first expressed, and then linear/angular velocity vectors are derived. In the notation, $j = 1, 2$ represents the first and second closed chains, respectively. Both chains have a passive revolute joint driven by a linear hydraulic actuator. Hence, we have:

$$q_1 = -2.0736 - \zeta_2, \quad q_2 = \zeta_3 - 0.4116, \quad (11)$$

$$x_j = \sqrt{L_j^2 + L_{j1}^2 + 2 L_j L_{j1} \cos q_j} - x_{j0}, \quad (12)$$

$$q_{j1} = -\arccos \left(\frac{L_{j1}^2 - (x_j + x_{j0})^2 - L_j^2}{-2(x_j + x_{j0}) L_j} \right), \quad (13)$$

$$q_{j2} = -\arccos \left(\frac{L_j^2 - (x_j + x_{j0})^2 - L_{j1}^2}{-2(x_j + x_{j0}) L_{j1}} \right), \quad (14)$$

where L_j and L_{j1} are lengths between the frames, and x_{j0} is the effective length of the hydraulic linear actuator at zero piston stroke. Differentiating (12)–(14) and appropriately transforming them result in:

$$\dot{x}_j = -\frac{L_j L_{j1} \sin q_j}{x_j + x_{j0}} \dot{q}_j, \quad (15)$$

$$\dot{q}_{j1} = -\frac{(x_j + x_{j0}) - L_j \cos q_{j1}}{(x_j + x_{j0}) L_j \sin q_{j1}} \dot{x}_j, \quad (16)$$

$$\dot{q}_{j2} = -\frac{(x_j + x_{j0}) - L_{j1} \cos q_{j2}}{(x_j + x_{j0}) L_{j1} \sin q_{j2}} \dot{x}_j. \quad (17)$$

with $\dot{q}_1 = \dot{\zeta}_2$ and $\dot{q}_2 = \dot{\zeta}_3$. The equations in (11)–(17) reveal the relations between passive joint angle motion and corresponding piston motion. Through these relations, one can control the revolute joint angle by controlling the piston position. Exploiting VCP, closed chains in object 2 are decomposed into subsystems (shown in Fig. 3) through open chains, such that the linear/angular velocities in the open kinematic chain $1j$ and $2j$ can be written as:

$${}^{B_{1j}} V = z_\tau \dot{q}_j + {}^{B_{0j}} U_{B_{1j}}^T {}^{B_{0j}} V, \quad (18)$$

$${}^{T_{1j}} V = {}^{B_{1j}} U_{T_{1j}}^T {}^{B_{1j}} V, \quad (19)$$

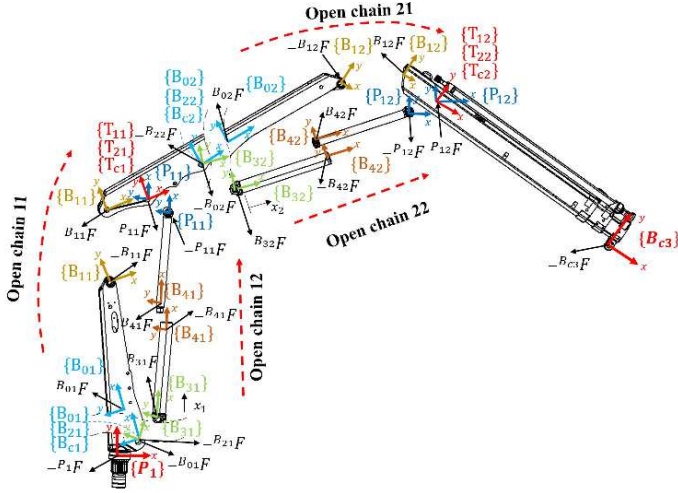


Fig. 3. VDC frames of object 2

$$B_{3j}V = z_\tau \dot{q}_{j1} + B_{2j}U_{B_{3j}}^T B_{2j}V, \quad (20)$$

$$B_{4j}V = x_f \dot{x}_j + B_{3j}U_{B_{4j}}^T B_{3j}V, \quad (21)$$

$$T_{2j}V = z_\tau \dot{q}_{j2} + B_{4j}U_{T_{2j}}^T B_{4j}V. \quad (22)$$

Considering Fig. 3, linear/angular velocities at the driving VCP of the closed kinematic chains are:

$$T_{c2}V = T_{1j}V = T_{2j}V. \quad (23)$$

Note that, from Fig. 3, we have:

$$B_{c1}V = P_1U_{B_{c1}}^T P_1V, \quad (24)$$

$$B_{c2}V = T_{c1}U_{B_{c2}}^T T_{c1}V, \quad (25)$$

$$B_{c3}V = B_{0j}V = B_{2j}V. \quad (26)$$

Finally, linear/angular velocities measured and expressed in frame $\{B_{c3}\}$ of object 2 can be calculated as:

$$B_{c3}V = T_{c2}U_{B_{c3}}^T T_{c2}V. \quad (27)$$

Therefore, all the linear/angular velocity vectors of object 2 are computed.

3) *Kinematics of Object 3*: Object 3 consists of three rotary hydraulic actuators (RHAs), as demonstrated in Fig. 4. For the sake of the compact computation, $i = 1, 2, 3$ attributes to the first, second, and third rotary actuators, respectively. Accordingly, considering Fig. 4, we have:

$$G_iV = \varrho_i \dot{\xi}_i + E_iU_{G_i}^T E_iV, \quad (28)$$

$$E_{i+1}V = G_iU_{E_{i+1}}^T G_iV. \quad (29)$$

with $E_1V = B_{c3}V$, and $\varrho_{1,3} = x_f$ and $\varrho_2 = y_f$. Moreover, $E^iV = E^iU_E^T E^iV$ is the linear/angular velocity of the end-effector. It must be mentioned that the angular velocity of each joint of object 3 has the following relation with piston displacement inside the hydraulic rotary actuator:

$$\dot{x}_{wi} = r_{wi} \dot{\xi}_i. \quad (30)$$

with r_{wi} being gear ratio.

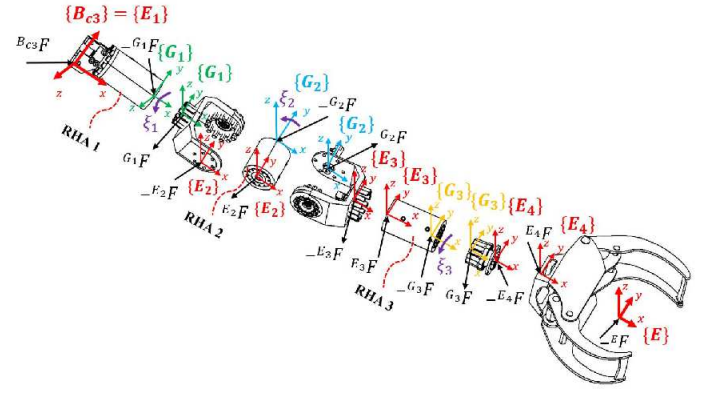


Fig. 4. VDC frames of object 3. RHA is the abbreviation for rotary hydraulic actuator.

B. Dynamics of the Manipulator

In this section, the total force/moment vectors exerted on each rigid body in each object are derived. The net forces in (4) can be computed for each rigid body by replacing $\{A\}$ with the corresponding frame. In order to consider the unknown disturbance and unknown model uncertainty, we can rewrite (4) as:

$$M_A \frac{d}{dt} ({}^A V) + C_A ({}^A \omega) {}^A V + G_A + {}^A \Delta_R(t) = {}^A F^* - {}^A D(t) \quad (31)$$

where ${}^A \Delta_R(t)$ and ${}^A D(t)$ satisfy Assumption 1 and being unmodeled dynamics and disturbances, respectively.

1) *Dynamics of Object 3*: The net force/moment vector of object 3 in Fig. 4 can be expressed as:

$$G_i F^* = G_i F - G_i U_{E_{i+1}} E_{i+1} F. \quad (32)$$

which enables us to compute $G_i F$:

$$G_i F = G_i F^* + G_i U_{E_{i+1}} E_{i+1} F. \quad (33)$$

In the same way, one can write:

$$E_i F = E_i F^* + E_i U_{G_i} G_i F. \quad (34)$$

for $i = 3, 2, 1$. The $E^i F = E^i U_E E^i F$ with $E^i F$ is the force/moment sensed from the environment. Consequently, the linear piston force in RHAs can be computed as:

$$f_{cwi} = \frac{1}{r_{wi}} \varrho_i^T G_i F + \varrho_i^T G_{pi} F^*. \quad (35)$$

In (35), the first term indicates the piston force that must overcome rigid body forces, and the second term computes the inertial effect of the piston body.

2) *Dynamics of Object 2*: The dynamics of the open kinematic chain $2j$ can be represented as:

$$B_{4j} F = B_{4j} F^* + B_{4j} U_{P_{1j}} P_{1j} F, \quad (36)$$

$$B_{3j} F = B_{3j} F^* + B_{3j} U_{B_{4j}} B_{4j} F, \quad (37)$$

$$B_{2j} F = B_{2j} U_{B_{3j}} B_{3j} F. \quad (38)$$

The dynamics of open chain $1j$ can be expressed in the same way as:

$$B_{1j} F = B_{1j} F^* + B_{1j} U_{B_{c_{j+1}}} B_{c_{j+1}} F - B_{1j} U_{P_{1j}} P_{1j} F. \quad (39)$$

$${}^{B_{0j}}F = {}^{B_{0j}}F^* + {}^{B_{0j}}U_{B_{1j}} {}^{B_{1j}}F. \quad (40)$$

where ${}^{B_{c3}}F = {}^{E_1}F$. Considering (36)-(40) and provoking theorems 3 and 4 of [6], the force/moment vector at the driven VCP along with linear actuator force of the parallel-serial joints in object 2, can be derived as:

$${}^{B_{c3}}F = {}^{B_{0j}}F^* + {}^{B_{0j}}U_{B_{1j}} {}^{B_{1j}}F^* + {}^{B_{2j}}U_{B_{3j}} {}^{B_{3j}}F^* + {}^{B_{2j}}U_{B_{3j}} {}^{B_{3j}}U_{B_{4j}} {}^{B_{4j}}F^* + {}^{B_{0j}}U_{B_{1j}} {}^{B_{1j}}U_{E_{1j}} {}^{E_{1j}}F \quad (41)$$

$$f_{cj} = \frac{x_f^T {}^{B_{4j}}F^* - \frac{z_\tau^T ({}^{B_{1j}}F^* + {}^{B_{1j}}U_{E_{1j}} {}^{E_{1j}}F)}{L_{j1} \sin q_{j2}}}{\frac{z_\tau^T ({}^{B_{3j}}F^*) + z_\tau^T ({}^{B_{4j}}F^*)}{(x_j + x_{j0}) \tan q_{j2}} - \frac{y_f^T ({}^{B_{4j}}F^*) (x_j + x_{j0} - l_{cj})}{(x_j + x_{j0}) \tan q_{j2}}}. \quad (42)$$

Now, with having ${}^{B_{c1}}F$, the dynamics of the object 1 can be derived.

Corollary 1: The following expressions can be written and assumed to be valid:

$$z_\tau^T {}^{B_{1j}}F = 0, \quad (43)$$

$$z_\tau^T {}^{P_{1j}}F = 0, \quad (44)$$

$$z_\tau^T {}^{B_{3j}}F = 0. \quad (45)$$

3) *Dynamics of Object 1:* Having ${}^{B_{c1}}F$ from object 2 and considering Fig. 3, one can obtain the force/moment vector of the pillar as:

$${}^{P_1}F = {}^{P_1}F^* + {}^{P_1}U_{B_{c1}} {}^{B_{c1}}F. \quad (46)$$

which results in linear piston force in object 1 as below:

$$f_{cp} = \frac{1}{r_p} y_\tau^T {}^{P_1}F + x_f^T {}^{P_{p2}}F^*. \quad (47)$$

${}^{P_{p2}}F^*$ is the net force/moment vector of the piston body.

IV. CONTROL DESIGN OF THE RIGID BODY SUBSYSTEM

In this section, for the modeled 6-DoF HHM, the procedure of local controller design is expressed. The VDC approach enables us to design local controllers that accomplish the local goals, and then by employing VPF, the main objective of the system is achieved by orchestrating all the local controllers.

A. Desired Trajectory

To determine the precise motion of HHMs in Cartesian space, it is critical to have a robust and precise controller at the actuator level. The kinematic relation between the Cartesian space and joint space for the 6-DoF manipulator can be written as:

$$\dot{\Pi}_d = J \dot{\Theta}_d \quad (48)$$

with $\dot{\Pi}_d = [\dot{X}_d, \dot{Y}_d, \dot{Z}_d, \dot{\omega}_{xd}, \dot{\omega}_{yd}, \dot{\omega}_{zd}]^T$ being desired pose velocity of the end-effector, $\dot{\Theta}_d = [\dot{\zeta}_{1d}, \dot{\zeta}_{2d}, \dot{\zeta}_{3d}, \dot{\xi}_{1d}, \dot{\xi}_{2d}, \dot{\xi}_{3d}]^T$ being desired angular velocity, and $J \in \mathbb{R}^{6 \times 6}$ is the Jacobian matrix. Therefore, the joint space velocity can be computed as:

$$\dot{\Theta}_d = J^{-1} \dot{\Pi}_d. \quad (49)$$

It can be seen from (49) that the desired trajectory of working space can be projected onto a joint space trajectory. It means that precise joint control will end up with precise end-effector pose control. This study aims to design a precise controller to achieve a considerably low tracking error.

B. Required Velocity Vectors

By solving the inverse kinematic problem in (49), the desired angular velocity and desired joint angle can be computed. Then, the required angular velocity in the sense of (6) can be derived. As expressed in (10) and (30), the linear motion is converted to angular motion through a constant parameter. However, the expression in (15) is complex and depends on the kinematics of the closed chain. Consequently, we define the required velocity of objects 1 and 3 based on the angular motion, and for object 2 based on piston motion. It is straightforward to compute the desired piston velocity and position for object 2 using (49), (11), (12), and (15) by replacing the actual signals with desired ones. Therefore, the required joint velocities can be defined as:

$$\dot{\zeta}_{1r} = \dot{\zeta}_{1d} + \lambda (\zeta_{1d} - \zeta_1), \quad (50)$$

$$\dot{x}_{jr} = \dot{x}_{jd} + \bar{\lambda}_{xj} (x_{jd} - x_j), \quad (51)$$

$$\dot{\xi}_{ir} = \dot{\xi}_{id} + \sigma_i (\xi_{1d} - \xi_i), \quad (52)$$

with $j = 1, 2, i = 1, 2, 3$, and $\lambda, \bar{\lambda}_{xj}$, and σ_i are constant positive gains. By replacing (50)-(52) in the kinematic part of each object and reusing (10), (15)-(17), and (30), the required linear/angular velocities can be achieved as:

$${}^{P_1}V_r = {}^G U_{P_1}^T {}^G V_r + y_\tau \dot{\zeta}_{1r} \quad (53)$$

$${}^{P_{p2}}V_r = {}^{P_{p1}}U_{P_{p2}}^T {}^{P_{p1}}V_r + x_f \dot{x}_{pr} \quad (54)$$

$${}^{B_{1j}}V_r = z_\tau \dot{q}_{jr} + {}^{B_{0j}}U_{B_{1j}}^T {}^{B_{0j}}V_r, \quad (55)$$

$${}^{T_{1j}}V_r = {}^{B_{1j}}U_{T_{1j}}^T {}^{B_{1j}}V_r, \quad (56)$$

$${}^{B_{3j}}V_r = z_\tau \dot{q}_{j1r} + {}^{B_{2j}}U_{B_{3j}}^T {}^{B_{2j}}V_r, \quad (57)$$

$${}^{B_{4j}}V_r = x_f \dot{x}_{jr} + {}^{B_{3j}}U_{B_{4j}}^T {}^{B_{3j}}V_r, \quad (58)$$

$${}^{T_{2j}}V_r = z_\tau \dot{q}_{j2r} + {}^{B_{4j}}U_{T_{2j}}^T {}^{B_{4j}}V_r. \quad (59)$$

$${}^{B_{c1}}V_r = {}^{P_1}U_{B_{c1}}^T {}^{P_1}V_r, \quad (60)$$

$${}^{B_{c2}}V_r = {}^{T_{c1}}U_{B_{c2}}^T {}^{T_{c1}}V_r, \quad (61)$$

$${}^{B_{c3}}V_r = {}^{T_{c2}}U_{B_{c3}}^T {}^{T_{c2}}V_r. \quad (62)$$

$${}^{G_i}V_r = \varrho_i \dot{\xi}_{ir} + {}^{E_i}U_{G_i}^T {}^{E_i}V_r, \quad (63)$$

$${}^{E_{i+1}}V_r = {}^{G_i}U_{E_{i+1}}^T {}^{G_i}V_r. \quad (64)$$

The required joint velocities in (50)-(52) show the required trajectory that each joint must follow in order to achieve the local control objectives. On the other side, the required linear/angular velocity vectors in (53)-(64) display the velocity that the rigid body should acquire to track the desired motion. In the following, the local controller will be designed in a way that provides the required effort to establish the desired motion.

C. Required Force Vectors

The required force/moment vector must be robust in the presence of model uncertainty and external disturbances. Therefore, considering the presented model in (31), the required net force/moment vector can be designed in the sense of (7) by taking advantage of (5) as:

$${}^A F_r^* = Y_A \hat{\phi}_A + K_A ({}^A V_r - {}^A V) + {}^A \Delta_R + {}^A D(t). \quad (65)$$

However, the model uncertainty ${}^A \Delta_R$ is unknown in real-world applications. Additionally, the magnitude and frequency of the external disturbances are unknown for many applications, especially for industrial manipulators. In this study, adaptive control and DRBFNN approaches are utilized to address the mentioned issues. According to Lemma 1, we can define:

$${}^A \Delta_R = {}^A W^T \Psi(\chi_A) + {}^A \varepsilon^* \quad (66)$$

where ${}^A W \in \mathbb{R}^{6 \times \bar{n}_A}$ is the RBFNNs weight, $\Psi(\cdot)$ is Gaussian activation function, $\chi_A = [{}^A V^T, {}^A V_r^T, {}^A \dot{V}_r^T]^T \in \mathbb{R}^{18}$, ${}^A \varepsilon^* \in \mathbb{R}^6$ is the RBFNNs approximation error, and \bar{n}_A is the number of neurons in rigid body subsystem $\{A\}$. By changing \bar{n}_A , one can set different numbers of nodes for different rigid body subsystems. Since the actual values for ${}^A W$ and ${}^A \varepsilon^*$ are not available, their estimations, denoted ${}^A \hat{W}$ and ${}^A \hat{\varepsilon}^*$ are utilized in the control design. By defining ${}^A \varepsilon = {}^A \hat{\varepsilon}^* + {}^A D(t)$, we can rewrite (65) as:

$${}^A F_r^* = Y_A \hat{\phi}_A + K_A ({}^A V_r - {}^A V) + {}^A \hat{W}^T \Psi(\chi_A) + {}^A \hat{\varepsilon} \quad (67)$$

with ${}^A \hat{\varepsilon}$ being the estimation of ${}^A \varepsilon$. In (67), the term ${}^A \hat{\varepsilon}$ estimates both the bias of the RBFNNs ${}^A \varepsilon^*$ and the external disturbance $D(t)$. Then, the required force/moment vectors can be computed by evoking force/moment vectors and using (67) as:

$$G_i F_r = G_i F_r^* + G_i U_{E_{i+1}} E_{i+1} F_r \quad (68)$$

$$E_i F_r = E_i F_r^* + E_i U_{G_i} G_i F_r \quad (69)$$

$$B_{1j} F_r = B_{1j} F_r^* + B_{1j} U_{B_{c,j+1}} B_{c,j+1} F_r - B_{1j} U_{P_{1j}} P_{1j} F_r. \quad (70)$$

$$B_{0j} F_r = B_{0j} F_r^* + B_{0j} U_{B_{1j}} B_{1j} F_r. \quad (71)$$

$$\begin{aligned} B_{cj} F_r = & B_{0j} F_r^* + B_{0j} U_{B_{1j}} B_{1j} F_r^* + B_{2j} U_{B_{3j}} B_{3j} F_r^* \\ & + B_{2j} U_{B_{3j}} B_{3j} U_{B_{4j}} B_{4j} F_r^* \\ & + B_{0j} U_{B_{1j}} B_{1j} U_{E_{1j}} E_{1j} F_r \end{aligned} \quad (72)$$

$$P_1 F_r = P_1 F_r^* + P_1 U_{B_{c1}} B_{c1} F_r \quad (73)$$

with $i = 3, 2, 1$ and $j = 2, 1$. Finally, the required piston forces that must be applied at the actuator level in order to accomplish the control objective can be derived as:

$$f_{cwir} = \frac{1}{r_{wi}} \varrho_i^T G_i F_r + \varrho_i^T G_{pi} F_r^* \quad (74)$$

$$\begin{aligned} f_{cjr} = & x_f^T B_{4j} F_r^* - \frac{z_\tau^T (B_{1j} F_r^* + B_{1j} U_{E_{1j}} E_{1j} F_r)}{L_{j1} \sin q_{j2}} \\ & - \frac{z_\tau^T (B_{3j} F_r^*) + z_\tau^T (B_{4j} F_r^*)}{(x_j + x_{j0}) \tan q_{j2}} \\ & + \frac{y_f^T (B_{4j} F_r^*) (x_j + x_{j0} - l_{cj})}{(x_j + x_{j0}) \tan q_{j2}} \end{aligned} \quad (75)$$

$$f_{cpr} = \frac{1}{r_p} y_\tau^T P_1 F_r + x_f^T P_{p1} F_r^*. \quad (76)$$

Remark 1: The control laws in (74)-(76) have three local goals: i) canceling the inertial effect of the rigid body, ii) compensating for unknown disturbances and model uncertainty, and iii) having a precise trajectory tracking. As demonstrated, the required action for the rigid body part and actuator part are computed separately, avoiding coupling nonlinearities. However, the required actuator force in (74)-(76) encompasses the rigid body-joint coupling nonlinearities, a significant feature of VDC that deals with each subsystem separately.

In the following section, taking into account the complex and nonlinear model of the hydraulic actuator, the low-level controller is designed to ensure the required forces in (74)-(76) will be generated at the actuator level. Since the procedure of modeling for all the hydraulic actuators in this study is the same, we derived the required voltage for a given linear piston force f_c , similar to (35), (42), and (47), and required piston force f_{cr} as in (74)-(76).

V. MODELING AND CONTROL OF ACTUATOR SUBSYSTEM

In this section, first, for a given desired voltage u_d^* and voltage applied to the system in the presence of deadzone-backlash nonlinearity u^* , the error $u^* - u_d^*$ is derived which later will be incorporated into stability analysis to ensure robustness and to handle parameter uncertainties. Then, the required voltage is computed for a given required piston force.

A. Inverse Deadzone-Backlash

Input constraints must be considered in control design to ensure control signals remain within safe and feasible bounds. Ignoring input constraints can lead to issues, such as system instability, equipment damage, and safety hazards, especially in real-world applications. The compound input constraint, that is deadzone and backlash, is examined in this section. Suppose that u_d^* is a control signal that may accomplish control objectives in the absence of input constraints, while v^* is the control signal with deadzone-backlash compensation. The deadzone function can be defined as,

$$v_1 = DZ(v^*) = \begin{cases} m_d(v^* - b_r), & v^* \geq b_r, \\ 0, & b_l < v^* < b_r \\ m_d(v^* - b_l), & v^* \leq b_l \end{cases} \quad (77)$$

with $m_d > 0$, $b_r > 0$, and $b_l < 0$ being deadzone parameters. Backlash function can be defined as,

$$u^* = BS(v_1) = \begin{cases} k_b(v_1 - B_r), & \dot{v}_1 > 0, \\ k_b(v_1 - B_l), & \dot{v}_1 < 0 \\ u^*(t_-), & \text{otherwise} \end{cases} \quad (78)$$

with $k_b > 0$, $B_r > 0$, and $B_l < 0$ being backlash parameters. By substituting (77) in (78), one can obtain,

$$u^* = DB(v^*) = \begin{cases} c(v^* - b_r) - d_r, & \dot{v}_1 > 0 \ \& \ v^* \geq b_r \\ -d_r, & \dot{v}_1 > 0 \ \& \ b_l < v^* < b_r \\ c(v^* - b_l) - d_r, & \dot{v}_1 > 0 \ \& \ v^* \leq b_l \\ c(v^* - b_r) - d_l, & \dot{v}_1 < 0 \ \& \ v^* \geq b_r, \\ -d_l, & \dot{v}_1 < 0 \ \& \ b_l < v^* < b_r \\ c(v^* - b_l) - d_l, & \dot{v}_1 < 0 \ \& \ v^* \leq b_l \\ u^*(t_-), & otherwise \end{cases} \quad (79)$$

After designing the control voltage in the absence of compound input constraint (79), the control law can be enhanced to cancel the damaging effect of such a constraint, such that $u_d^* = DB(DBI(u_d^*))$ with $DBI(\cdot)$ being the inverse deadzone-backlash function. On the other hand, in real-world applications, the parameters in (79) are unknown, and, it is desirable to estimate them. Consequently, we can write the adaptive inverse deadzone-backlash control term as,

$$v^* = \frac{1}{\hat{c}} u_d^* + \tilde{w}(t) \quad (80)$$

with

$$\hat{w}(t) = \begin{cases} \frac{\hat{d}_r}{\hat{c}} + \hat{b}_r, & \dot{u}_d^* > 0 \ \& \ u_d^* > 0, \\ \frac{\hat{d}_r}{\hat{c}} + \hat{b}_l, & \dot{u}_d^* > 0 \ \& \ u_d^* < 0 \\ \frac{\hat{d}_l}{\hat{c}} + \hat{b}_r, & \dot{u}_d^* < 0 \ \& \ u_d^* > 0, \\ \frac{\hat{d}_l}{\hat{c}} + \hat{b}_l, & \dot{u}_d^* < 0 \ \& \ u_d^* < 0, \\ w(t_-) & otherwise. \end{cases} \quad (81)$$

As the signal $\hat{w}(t)$ in (81) is discontinuous when \dot{u}_d^* and u_d^* changes the sign, we utilize the following differential equation as a continuous approximation of $\hat{w}(t)$ [26], which is used in (80):

$$\dot{\hat{w}}(t) = \alpha(-\hat{w}(t) + \hat{w}(t)) \quad (82)$$

with $\alpha > 0$ and $\hat{w}(0) \in [\frac{\hat{d}_l}{\hat{c}} + \hat{b}_l, \frac{\hat{d}_r}{\hat{c}} + \hat{b}_r]$, and \hat{c} , \hat{d}_r , \hat{d}_l , \hat{b}_r , and \hat{b}_l being the estimation of c , d_r , d_l , b_r , and b_l , respectively. Further, to derive an adaptation law for the estimation of unknown parameters we need to parameterize the control error $u^* - u_d^*$ utilizing (79) and (80). To do so, (80) can be rewritten as,

$$v^*(t) = \frac{1}{\hat{c}} (u_d^* + \varphi(\dot{u}_d^*) \hat{d}_r + \varphi(-\dot{u}_d^*) \hat{d}_l) + \varphi(u_d^*) \hat{b}_r + \varphi(-u_d^*) \hat{b}_l \quad (83)$$

where the smooth function $\varphi(\kappa) = (\tanh([\kappa - \kappa_0]/x_0) + 1)/2$, with κ_0 and x_0 being small constants, is utilized to compensate for the chattering resulting from discontinuity in (80). Considering $\hat{\theta} = [\hat{c}, \hat{c}b_r, \hat{c}b_l, \hat{d}_r, \hat{d}_l]^T$ with $\hat{b}_r = \hat{c}b_r/\hat{c}$, $\hat{b}_l = \hat{c}b_l/\hat{c}$, $\eta = [-v, \varphi(\dot{u}_d^*), \varphi(-\dot{u}_d^*), \varphi(u_d^*), \varphi(-u_d^*)]^T$, (83) can be written in parameterized way:

$$u_d^*(t) = -\hat{\theta}^T \eta. \quad (84)$$

Subsequently, the adaptive deadzone-backlash inverse error can be written as,

$$u^*(t) - u_d^*(t) = -(\theta - \hat{\theta})^T \eta + \eta_0 = -\tilde{\theta}^T \eta + \eta_0. \quad (85)$$

with η_0 being the bound mismatch error, $u^*(t)$ being the signal after deadzone-backlash, $u_d^*(t)$ being the desired signal in the

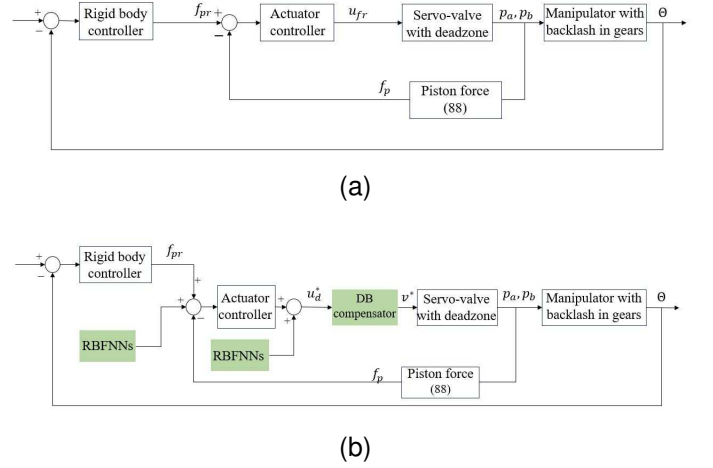


Fig. 5. a) The closed-loop scheme of the original VDC in the presence of compound input constraint and unknown model and actuator uncertainties, b) proposed method with deadzone-backlash and uncertainty compensator

absence of deadzone-backlash, and $\tilde{\theta}$ being the estimation error of the constraint parameters. To guarantee robustness and better performance, the parameter and model uncertainties of the compound input constraint can be tackled by designing an adaptation law for $\hat{\theta}$ and RBFNNs for estimation of η_0 , which will be addressed later. Fig. 5 displays the closed-loop scheme of the original VDC and the proposed method. As it is shown in Fig. 5b the deadzone-backlash compensator is incorporated into the controller to assure robustness and better performance in comparison to the original VDC, shown in Fig. 5a.

Remark 2: The deadzone-backlash compensation error in (85) is general for any system that is subjected to such a compound constraint. Therefore, it can be incorporated into any control law at the force/torque and voltage levels to cancel the input constraint.

B. Hydraulic actuator dynamics and control

As mentioned in Assumption 2, only the friction between the piston and the cylinder in the hydraulic actuator is considered, as it significantly impacts actuator performance. In this study, the model proposed in [11] is utilized to tackle the friction:

$$f_f = Y_f \phi_f \quad (86)$$

where $Y_f \in \mathbb{R}^{1 \times 7}$ is the regressor matrix and $\phi_f \in \mathbb{R}^7$ is the friction parameter vector. The friction model in (86) includes coulomb friction, Stribeck friction, viscous friction, and the average deformation of the seal bristles, as well as a smooth transition between the presliding and sliding motions.

Now, considering the friction force and piston force, we have:

$$f_p = f_c + f_f. \quad (87)$$

On the other hand, the piston force can be computed using the chamber pressure, as:

$$f_p = A_a p_a - A_b p_b \quad (88)$$

with A_a and A_b being cross-sectional areas, and p_a and p_b being pressures in the hydraulic actuator chamber. The

cylinder chamber pressure can be generated by controlling the fluid flow rate entering the chamber. The equations of these fluid flow rates, denoted as Q_a and Q_b can be written as:

$$Q_a = c_{p1} v(p_s - p_a) u \mathcal{S}(u) + c_{n1} v(p_a - p_r) u \mathcal{S}(-u), \quad (89)$$

$$Q_b = -c_{n2} v(p_b - p_r) u \mathcal{S}(u) - c_{p2} v(p_s - p_b) u \mathcal{S}(-u), \quad (90)$$

where c_{p1} , c_{p2} , c_{n1} and c_{n2} are flow coefficients, p_s is the supply pressure, p_r is the return-line pressure, and $\mathcal{S}(u)$ is the selection function, defined as:

$$\mathcal{S}(u) = \begin{cases} 1, & \text{if } u > 0, \\ 0, & \text{if } u \leq 0, \end{cases} \quad (91)$$

and $v(\Delta p)$ is the function related to drops in pressure:

$$v(\Delta p) = \text{sign}(\Delta p) \sqrt{|\Delta p|}. \quad (92)$$

Employing continuity equations for hydraulic actuators, one can express the pressure dynamics in the cylinder chamber as:

$$\dot{p}_a = \frac{\beta}{V_{0a} + A_a x} (Q_a - A_a \dot{x} - Q_l), \quad (93)$$

and

$$\dot{p}_b = \frac{\beta}{V_{0b} + A_b(s-x)} (Q_b + A_b \dot{x} + Q_l), \quad (94)$$

where β denotes the oil bulk modulus, s is the maximum stroke of the piston, and the laminar leakage flow Q_l between the cylinder chambers is defined as:

$$Q_l = c_l(p_a - p_b), \quad (95)$$

with c_l being the leakage coefficient. Taking the time derivative of the (88) and recalling (89), (90), and (93)-(95), one can obtain:

$$\begin{aligned} \dot{f}_p &= \beta(u_f - \frac{A_a \dot{x}}{V_{0a}/A_a + x} - \frac{A_b \dot{x}}{V_{0b}/A_b + (s-x)}) \\ &\quad - c_l \frac{(p_a - p_b)(A_a V_{0b} + A_b V_{0a} + A_a A_b s)}{(V_{0a} + A_a x)(V_{0b} + A_b(s-x))} + \Delta_a \end{aligned} \quad (96)$$

with

$$u_f = -Y_v \theta_v + \Delta_a \quad (97)$$

where $Y_v = [Y_{v1}, Y_{v2}, Y_{v3}, Y_{v4}] \in \mathbb{R}^{1 \times 4}$ with $Y_{v1} = -\frac{v(p_s - p_a)}{V_{0a}/A_a + x} \mathcal{S}(u)u$, $Y_{v2} = -\frac{v(p_s - p_b)}{V_{0b}/A_b + (s-x)} \mathcal{S}(-u)u$, $Y_{v3} = -\frac{v(p_a - p_r)}{V_{0a}/A_a + x} \mathcal{S}(-u)u$, and $Y_{v4} = -\frac{v(p_b - p_r)}{V_{0b}/A_b + (s-x)} \mathcal{S}(u)u$, and $\theta_v = [c_{p1}, c_{p2}, c_{n1}, c_{n2}]^T \in \mathbb{R}^4$. Additionally, Δ_a is the unknown model uncertainty in the actuator dynamics.

Assumption 3: Pressures in linear hydraulic actuator chambers are always smaller than the supply pressure, and they are always higher than the return line pressure, which is never zero.

Assumption 3 provides univalence between u and u_f . It means that for the given u_f , a unique spool valve voltage signal u can be obtained as:

$$\begin{aligned} u &= \frac{u_f}{c_{p1} \frac{v(p_s - p_a)}{V_{0a}/A_a + x} + c_{n2} \frac{v(p_b - p_r)}{V_{0b}/A_b + (s-x)}} \mathcal{S}(u_f) \\ &\quad + \frac{u_f}{c_{n1} \frac{v(p_a - p_r)}{V_{0a}/A_a + x} + c_{p2} \frac{v(p_s - p_b)}{V_{0b}/A_b + (s-x)}} \mathcal{S}(-u_f). \end{aligned} \quad (98)$$

In order to ensure that the required piston force is generated at the actuator level, we need to design the voltage law u_{fr} . Considering (86), (87), (88), and (96) along with Lemma 1, we have:

$$f_{pr} = f_{cr} + Y_f \hat{\theta}_f, \quad (99)$$

$$u_{fr}^* = Y_d \hat{\theta}_d + k_f(f_{pr} - f_p) + k_x(\dot{x}_r - \dot{x}) + \hat{W}_a^T \Psi(\chi_a) + \hat{\varepsilon}_a, \quad (100)$$

with $\theta_d = [1/\beta, A_a, A_b, c_l]^T \in \mathbb{R}^4$, and $Y_d = [Y_{d1}, Y_{d2}, Y_{d3}, Y_{d4}] \in \mathbb{R}^{1 \times 4}$ with $Y_{d1} = \dot{f}_{pr}$, $Y_{d2} = \dot{x}/(V_{0a}/A_a + x)$, $Y_{d3} = \dot{x}/(V_{0b}/A_b + (s-x))$, and $Y_{d4} = ((p_a - p_b)(A_a V_{0b} + A_b V_{0a} + A_a A_b s))/((V_{0a} + A_a x)(V_{0b} + A_b(s-x)))$. Additionally, $\hat{W}_a \in \mathbb{R}^{\bar{n}_a \times 1}$ and $\hat{\varepsilon}_a \in \mathbb{R}$ are the estimation of W_a and $\varepsilon_a = \varepsilon_a^* + \eta_0$ in the sense of Lemma 1 to handle the unmodeled dynamics in the hydraulic actuator. η_0 is defined in (85) and \bar{n}_a is the total number of neurons in the actuator subsystem. The signal in (100) is the required voltage that accomplishes the control goals in the absence of deadzone-backlash, while u_{fr} is equipped with the input constraint compensator in the sense of (80) as:

$$u_{fr} = \frac{1}{\hat{c}} u_{fr}^* + \bar{w}(t) \quad (101)$$

Subsequently, the voltage error can be written in the sense of (85) as:

$$u_{fr} - u_{fr}^* = -\tilde{\theta}^T \eta + \eta_0 \quad (102)$$

where $u_{fr} = DB(v_{fr})$.

Therefore, by recalling (98), the spool valve control signal may written as:

$$\begin{aligned} u &= \frac{u_{fr} \mathcal{S}(u_{fr})}{\hat{c}_{p1} \frac{v(p_s - p_a)}{V_{0a}/A_a + x} + \hat{c}_{n2} \frac{v(p_b - p_r)}{V_{0b}/A_b + (s-x)}} \\ &\quad + \frac{u_{fr} \mathcal{S}(-u_{fr})}{\hat{c}_{n1} \frac{v(p_a - p_r)}{V_{0a}/A_a + x} + \hat{c}_{p2} \frac{v(p_s - p_b)}{V_{0b}/A_b + (s-x)}}. \end{aligned} \quad (103)$$

In order to estimate the flow coefficient in (103), we need to write it in the linear-in-parameter form. Therefore, as in (97), we can inversely write (103) as:

$$u_{fr} = -Y_v \hat{\theta}_v \quad (104)$$

with $(\hat{\cdot})$ being the estimation of (\cdot) . The low-level control law designed in (101) not only compensates for compound input constraints and unknown unmodeled dynamics at the actuator level, but it also makes the actuator produce the required piston forces that tackle unknown model uncertainty and unknown disturbances in rigid body part, resulting in precise trajectory tracking.

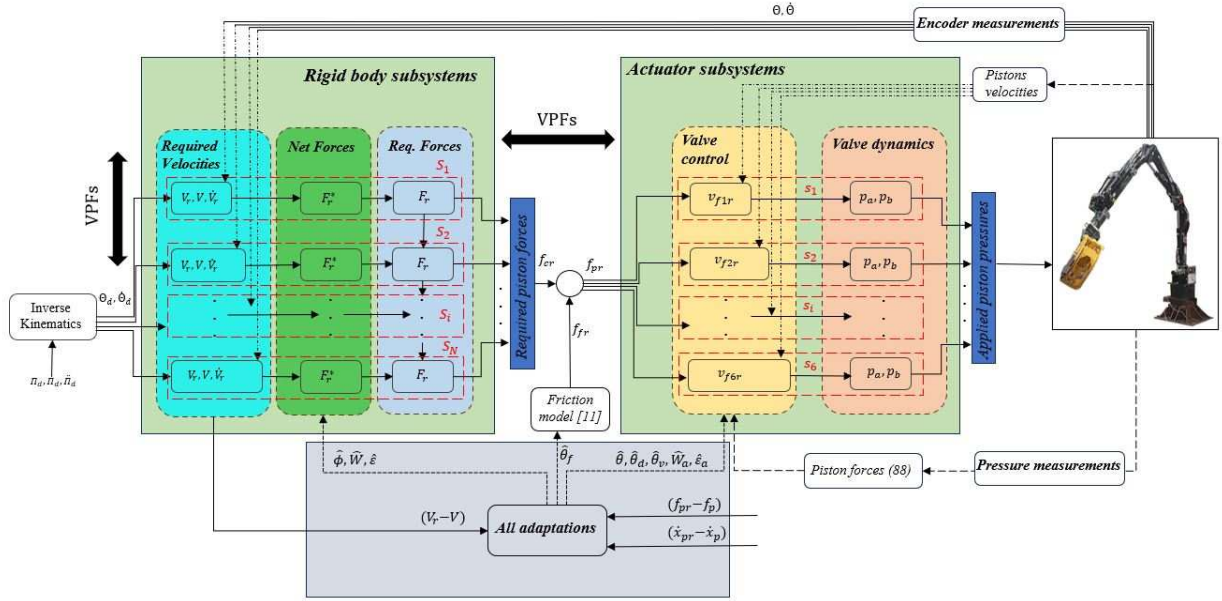


Fig. 6. General scheme of the orchestrated robust controller. f_{cr} is the required piston force that if applied to the rigid body, that subsystem will have the desired motion. v_{f_r} is the required low-level voltage that if applied to the valves, the actuator will produce f_{cr} . S_i is subsystems in the rigid body parts with N being the total number of rigid bodies, and s_i is a subsystem in the actuator level which is the same as the number of actuators.

VI. STABILITY ANALYSIS

In the previous section, the modeling and control of the HHM were established. Fig. 6 demonstrates the scheme of the proposed approach with details of subsystem-based modeling and control. Fig. 6 shows that the required force designed in the rigid body subsystem is transmitted to the actuator subsystem to be generated. The connections between rigid body subsystems and actuator subsystems are established by means of VPFs. In this section, the stability of the entire system under the proposed controller is analyzed. The adaptation functions for handling parameter uncertainties in rigid body parts and actuator parts are derived to achieve SGUUB.

Theorem 1: Consider the 6-DoF hydraulic manipulator demonstrated in Fig. 1 that decomposed into rigid body and actuator subsystems in Fig. 2-4. The rigid body dynamics (31) in the presence of unknown model uncertainty and disturbance under the robust local controller (67) with the adaptation law of:

$${}^A \dot{\hat{\mathcal{L}}} = \frac{1}{\gamma} {}^A \hat{\mathcal{L}} ({}^A \mathcal{S} - \gamma_0 {}^A \hat{\mathcal{L}}) {}^A \hat{\mathcal{L}} \quad (105)$$

$${}^A \dot{\hat{W}} = {}^A \Gamma (\Psi(\chi_A) ({}^A V_r - {}^A V)^T - {}^A \tau_0 {}^A \hat{W}) \quad (106)$$

$${}^A \dot{\hat{\varepsilon}} = {}^A \pi (({}^A V_r - {}^A V) - {}^A \pi_0 {}^A \hat{\varepsilon}), \quad (107)$$

is virtually stable, where $A \in S$ and $S = \{P_1, P_{p2}, B_{0j}, B_{1j}, B_{3j}, B_{4j}, G_i\}$ for $i = 1, 2, 3$ and $j = 1, 2$. Moreover, ${}^A \hat{\mathcal{L}}$ is the estimation of ${}^A \mathcal{L}$ defined in Lemma 2 and ${}^A \mathcal{S}$ is a unique symmetric matrix. The $\gamma, \gamma_0, \tau_0, \pi, \pi_0$ are positive constants, and Γ is a positive-definite matrix. Let the non-negative accompanying function for the rigid body part be chosen in the sense of Definition 3 as ν_1 . Then, the time derivative of ν_1 is:

$$\dot{\nu}_1 \leq -\alpha_1 \nu_1 + \alpha_{10} + VPFs \quad (108)$$

with α_1 and α_{10} being positive, and VPFs denoting the sum of driving and driven cutting points in the sense of Definition 1 and Definition 2.

Proof 1: The proof is provided in Appendix A.

Theorem 2: Consider the 6-DoF hydraulic manipulator demonstrated in Fig. 1 that decomposed into rigid body and actuator subsystems in Fig. 2-4. The actuator dynamics under the required piston forces (74), (75), and (76) with low-level voltage control signal (100) and (101) along with following adaptation functions:

$$\dot{\hat{\theta}}_{f(\cdot)} = \gamma_{f(\cdot)} \left(\frac{1}{k_{x(\cdot)}} Y_{f(\cdot)}^T (\dot{x}_{p(\cdot)r} - \dot{x}_{p(\cdot)}) - \gamma_{f(\cdot)0} \hat{\theta}_{f(\cdot)} \right) \quad (109)$$

$$\dot{\hat{\theta}}_{v(\cdot)} = \gamma_{v(\cdot)} \left(\frac{1}{k_{x(\cdot)}} Y_{v(\cdot)}^T (f_{p(\cdot)r} - f_{p(\cdot)}) - \gamma_{v(\cdot)0} \hat{\theta}_{v(\cdot)} \right) \quad (110)$$

$$\dot{\hat{\theta}}_{d(\cdot)} = \gamma_{d(\cdot)} \left(\frac{1}{k_{x(\cdot)}} Y_{d(\cdot)}^T (f_{p(\cdot)r} - f_{p(\cdot)}) - \gamma_{d(\cdot)0} \hat{\theta}_{d(\cdot)} \right) \quad (111)$$

$$\dot{\hat{\theta}}_{(\cdot)} = \delta_{(\cdot)} \left(\frac{1}{k_{x(\cdot)}} (f_{p(\cdot)r} - f_{p(\cdot)}) - \delta_{(\cdot)0} \hat{\theta}_{(\cdot)} \right) \quad (112)$$

$$\dot{\hat{W}}_{a(\cdot)} = \delta_{a(\cdot)} \left(\frac{1}{k_{x(\cdot)}} (f_{p(\cdot)r} - f_{p(\cdot)}) \Psi(\chi_{a(\cdot)}) - \delta_{a(\cdot)0} \hat{W}_{a(\cdot)} \right) \quad (113)$$

$$\dot{\hat{\varepsilon}}_{a(\cdot)} = \bar{\delta}_{a(\cdot)} \left(\frac{1}{k_{x(\cdot)}} (f_{p(\cdot)r} - f_{p(\cdot)}) - \bar{\delta}_{a(\cdot)0} \hat{\varepsilon}_{a(\cdot)} \right) \quad (114)$$

is virtually stable, with (\cdot) denoting all the objects. Defining the non-negative accompanying functions for linear hydraulic actuators as ν_a in the sense of Definition 3 yields to:

$$\dot{\nu}_a \leq -\mu_a \nu_a + \mu_{a0} + VPFs \quad (115)$$

with μ_a and μ_{a0} being positive, and VPFs being the virtual cutting points at the actuator level.

Proof 2: The proof is provided in Appendix B.

Theorem 3: Consider the entire 6-DoF heavy-duty hydraulic manipulator with rigid body and actuator dynamics represented in (31)-(47) and (86)-(98) with control laws of (67), (74), (75), (76), (100), and (101) and adaptation functions in (105)-(107) and (109)-(114). All the signals and errors in the system are SGUUB and will remain within a compact set. For example, velocity tracking error, actuator force tracking error, and RBFNNs weight estimation error will stay within a compact set Ω_V , Ω_f , and Ω_W , respectively, where $\Omega_V = \{e_V \in \mathbb{R}^6 \mid \|e_v\| \leq \sqrt{\frac{2B}{\lambda_{\min}(M)}}\}$, $\Omega_f = \{e_f \in \mathbb{R} \mid \|e_f\| \leq \sqrt{2B\beta k_x}\}$, and $\Omega_W = \{\tilde{W}_a \in \mathbb{R}^n \mid \|\tilde{W}_a\| \leq \sqrt{2B\delta_x}\}$ with $B = \bar{\mu}_0/\bar{\mu}$. Similarly, for all the errors, a compact set can be achieved.

Proof 3: The proof is provided in Appendix C.

VII. RESULTS AND DISCUSSION

In this section, the simulation and experimental results are provided to evaluate the performance of the proposed controller. First, the simulation results of comparing the presented method with three different controllers, including the original VDC, proportional-differential (PD) controller, and the state-of-the-art controller, adaptive dynamic surface controller with funnel control and neural networks (ADSC-FC-NN) proposed in [16]. The simulation analysis is performed for the base joint of the HHM, shown in Fig. 1, which is subjected to deadzone in valves and backlash in the rack and pinion mechanism. Then, the performance of the proposed method is implemented to control the real-world commercial heavy-duty hydraulic manipulator. The RVDC in the figures is an abbreviation for robust VDC, which represents the presented method.

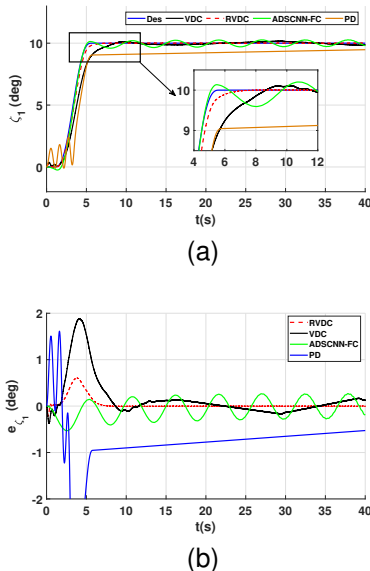


Fig. 7. a) The simulation result of tracking of a desired trajectory with four different controllers for the base joint, b) time history of the corresponding errors.

A. Performance comparison in Simulation

In the simulation, which is performed by MATLAB & SIMULINK, the deadzone and backlash constraints are considered to evaluate the performance of each controller in the

presence of such compound constraints, as well as model uncertainties. The deadzone and backlash parameters are set to $b_r = -b_l = 0.2$, $m_d = 1$, $B_r = -B_l = 0.2$, $k_b = 1$. All the control gains are tuned to achieve the best results for each controller, and the 10 nodes in total are utilized for RBFNNs in the proposed method and ADSC-FC-NN. Fig. 7 demonstrates the result of the simulation. The desired trajectory in Fig. 7a helps to analyze both the transient and steady-state performances of each controller. As displayed in the figure, the ADSC-FC-NN controller has much better transient performance than the original VDC and PD. However, both the VDC and ADSC-FC-NN could not converge to the desired point, and both oscillated around the set point, with errors of 0.17 and 0.25 degrees, respectively, due to the compound input constraint. This shows that the RBFNN in ADSC-FC-NN could not perfectly estimate the uncertainty in the actuator. In contrast, the proposed method not only improved the weakness of the original VDC in the transient part, but it also ultimately converged to the desired point and perfectly tackled the effect of input constraints. Fig. 7b compares the errors of each controller. It can be concluded that using novel DRBFNNs for the estimation of actuator uncertainties, which estimation of the non-parametrizable term in (102) is part of it, based on the states of the actuator, perfectly accomplished the control objective. Table I additionally provides a quantitative performance evaluation of each controller by comparing the maximum-absolute of tracking error $|e_{max}|$, root-mean-square (RMS) error (RMSE) e_{rms} , and RMS of computed voltage u_{rms} . According to Table I, the maximum error value of the ADSC-FC-NN is better than the proposed method, while the designed controller has a much lower RMS error and almost zero steady-state error with lower voltage usage.

TABLE I
SIMULATION PERFORMANCE EVALUATION

Controller	PD	ADSC-NN-FC [16]	VDC	RVDC
$ e _{max} (^\circ)$	4.57	0.53	1.88	0.6
$e_{rms} (^\circ)$	1.04	0.22	0.46	0.12
$u_{rms} (v)$	0.15	0.74	0.34	0.44

B. Experimental Set-up

Fig. 8 demonstrates the experimental set-up for performance evaluation of the controller. In the following, the hardware components and properties are provided:

- Beckhoff and TwinCat 3 interface with a sample time of 1 ms
- Bosch Rexroth NG6 size servo solenoid valve with 12 l/min at $\Delta P = 3.5 MPa$ per notch for object 1, 100 l/min at $\Delta P = 3.5 MPa$ per notch for object 2, and 40 l/min at $\Delta P = 3.5 MPa$ per notch for object 3.
- Sick afs60 (18-bit) absolute encoders for all joint angle measurements.
- Eckart E3150-360 for first and third RHAs in object 3 and Eckart E3150-180 for second RHA (see Fig. 4).
- Druck PTX1400 and Unik 5000 pressure transmitters (range 25 MPa) for pressure measurements.

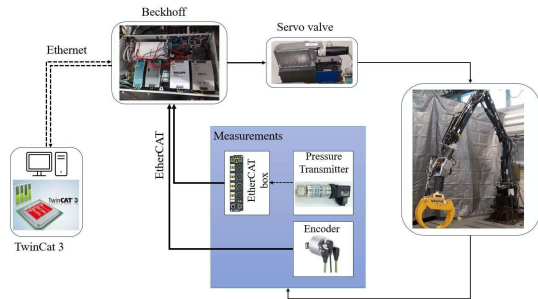


Fig. 8. Experimental set-up

- EP3174-0002 EtherCAT box for connecting pressure sensors to Beckhoff.

In order to implement the designed controller, only encoder and pressure sensor data are utilized. Using the pressure sensor to compute the piston force in (88) for automation of heavy-duty manipulators is a more practical solution since retrofitting the pressure sensors is much easier than retrofitting the piston load cell. In order to perform numerical differentiation for $\frac{d}{dt}({}^A V_r)$ in (67) and \dot{f}_{pr} and \dot{x}_p in (100), the finite difference method introduced in [39] is used with a low-pass filter. The control goal is to achieve five given set points in Cartesian space with the largest magnitude of 0.8 m , 1 m , and 1 m in x , y , and z directions, respectively, in different orientations. The Euler angles with the XYZ convention are used to represent the orientation of the end-effector with respect to the base, and the orientation error is computed based on the rotation matrix. Then, a smooth fifth-order trajectory generator [40] is utilized to produce a smooth trajectory between the set points for a given execution time, t_f . The (48) and (49) are used to compute the joint's desired values. Fig. 9 demonstrates the motion of the robot.

C. Experimental Result

In this section, the experimental results of implementing the proposed controller on an industrial 6-DoF HMM are provided. The result of the proposed method is compared to that of the original VDC controller to evaluate the control performance more accurately. Table II provides the control gains utilized in experiments. For the RBFNNs, the Gaussian activation function is defined as $\Psi(\chi) = \exp[-(\chi - c_j)^T(\chi - c_j)/(b_j^2)]$, with c_j and b_j denoting the center and width of the neural

TABLE II
CONTROL PARAMETERS FOR EXPERIMENT

Symbol	Value	Symbol	Value
λ	3	λ_{xj}	5
$\sigma_{1,2}$	12	σ_3	18
k_{xp}	0.02	k_{xj}	0.015
k_{xwi}	0.08	k_{fp}	$0.01 \cdot 10^{-8}$
k_{fj}	$2 \cdot 10^{-8}$	k_{fwi}	$1 \cdot 10^{-8}$
K_A	$50 \cdot \mathbf{I}$	γ	500
A_Γ	350	A_π	20
$\delta_{a(\cdot)}$	$1.5 \cdot k_{x(\cdot)} k_{f(\cdot)}$	$\bar{\delta}_{a(\cdot)}$	$0.5 \cdot k_{x(\cdot)} k_{f(\cdot)}$

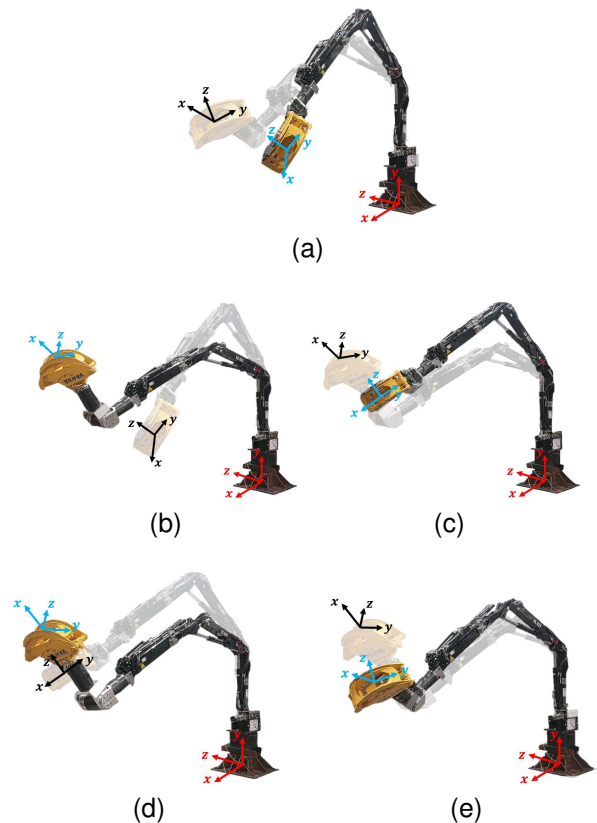


Fig. 9. Set-point reaching postures of the robot. Each image shows the transition from one set point to another. The end-effector is moving in the range of 4-5 meters reach.

cell in j th unit, with $\mathbf{j} = \bar{n}_A$ for rigid body subsystem, and $\mathbf{j} = \bar{n}_a$ for actuator subsystem. In this study the value for c_j is randomly selected in $[-1, 1]$ with $b_{\bar{n}_a} = 0.5$ and $b_{\bar{n}_A} = 5$ with the aggregation of used 270 nodes.

In Fig. 10, the performance of the proposed method and the original VDC in tracking a desired trajectory is compared. As demonstrated, both controllers performed excellently in following the desired trajectory. However, from Fig. 11, it can be concluded that the proposed controller achieved a much better result by handling the uncertainties in the model and considering the input constraints. As mentioned previously, the base and wrist actuators (objects 1 and 3) suffer from compound input constraints. Such uncertainty along with the model uncertainties lead to the steady-state error of 0.13, -0.6, -0.7, and 0.07 degree in ζ_1 , ξ_1 , ξ_2 , and ξ_3 , respectively, using VDC controller. By employing the presented controller, the errors are reduced to -0.04, -0.01, -0.02, and -0.01 degrees, respectively. In addition to the steady state errors, the proposed method achieved a considerably lower transient error, showing the perfect performance of the designed method in tackling unknown uncertainties and compound input constraints. Fig. 12, on the other hand, depicts the angular velocity of each joint along with the desired values, displaying that the RVDC ended up with much smoother tracking without jumps in velocities.

The lower force error ($\tilde{f} = f_{cr} - f_c$), shows the better performance of the hydraulic actuator in generating the required forces. Such a good performance of the actuator can be de-

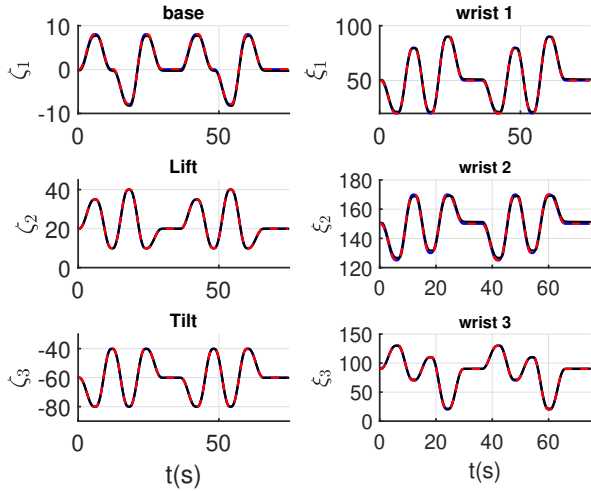


Fig. 10. Trajectory tracking of all six joints. The blue solid line is the desired trajectory, the dashed red line is with RVDC, and the black solid line is with VDC. The y-axis is in degrees.

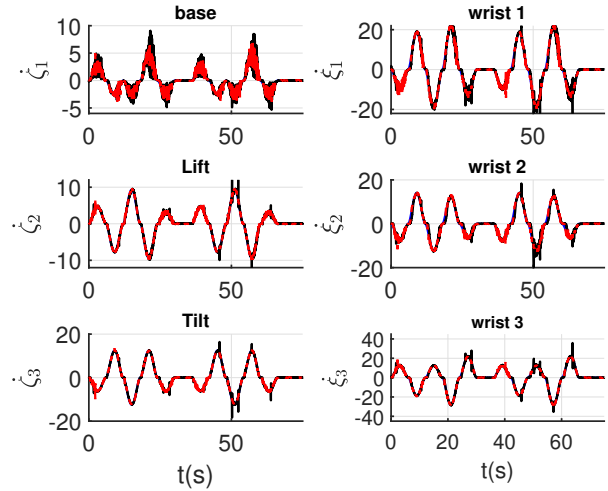


Fig. 12. Angular velocities of all joints. The blue solid line is the desired trajectory, the dashed red line is with RVDC, and the black solid line is with VDC. The y-axis is in degrees/sec.

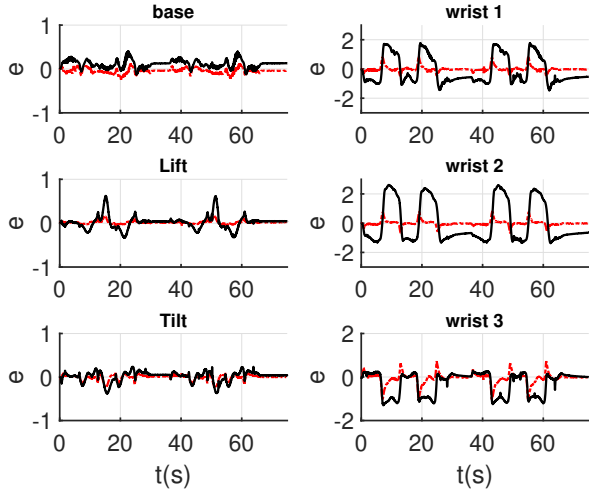


Fig. 11. Trajectory tracking error of each joint. The dashed red line is with RVDC, and the black solid line is with VDC. The y-axis is in degrees.

pendent on friction and model uncertainties. The experimental results of the actuator force tracking error are demonstrated in Fig. 13, from which can be seen that the actuator with RVDC had a much lower force error than VDC, displaying the impact of contributions of this study. Fig. 14, also, shows the time history of the estimated states. Fig. 14a shows the norm of all the estimated inertial parameter vectors of the rigid body in (67). Fig. 14b displays the estimated adaptive inverse deadzone-backlash parameters. Fig. 14c and 14d demonstrate the norm of estimation of weights and approximation errors of the DRBFNNs in rigid body subsystems. Finally, Fig. 14e and 14f, show the norm of estimated weights and approximation error in the actuator subsystems. All the presented figures show the boundedness of all signals and the good performance of the proposed method, validating the theoretical results. Table III summarizes the comparison between the original VDC and the proposed method. It can be seen that for a

TABLE III
PERFORMANCE EVALUATION

Controllers		B	L	T	W1	W2	W3
$e_{rms} (^{\circ})$	VDC	0.14	0.15	0.12	0.94	1.38	0.59
	RVDC	0.07	0.03	0.06	0.18	0.19	0.25
$ e _{max} (^{\circ})$	VDC	0.4	0.62	0.38	1.77	2.6	1.3
	RVDC	0.23	0.16	0.24	0.89	0.8	1.03
$\tilde{f}_{rms} (kN)$	VDC	15.3	2	1.13	31.53	44.82	31.5
	RVDC	13.3	3.1	1.2	16.74	19.4	18.9
$u_{rms} (v)$	VDC	0.7	0.6	0.55	0.53	0.4	0.62
	RVDC	0.51	0.56	0.55	0.51	0.41	0.62

given roughly the same power source, the proposed approach achieved considerably lower tracking errors in comparison to the original VDC [12], [36]. The generated actuator forces, also, with RVDC have a lower difference with the required value in contrast to the original VDC.

In order to check the sensitivity of the proposed controller to gain, three different experiments were performed with 70%, 90%, and 100% of the tuned gains. The RMSE of all joints was computed to compare the results. The total RMSE of joint tracking for 70%, 90%, and 100% are 0.455, 0.27, and 0.157, respectively. These results show that by setting different gains to the controller, it will remain stable, and only the tracking performance will be reduced. Therefore, the controller is robust to the changes in gains.

To examine the tracking performance of the controller in Cartesian space, the experimental results of the path following are provided in Fig. 15 for both the proposed method and the original VDC. As depicted in Fig. 15, the proposed method displayed better performance than the original VDC. The RMSE in the x , y , and z directions with VDC are 12.5 mm, 25 mm, and 12.5 mm, respectively, and with the proposed method, they are 2.5 mm, 3.2 mm, and 5.2 mm, respectively,

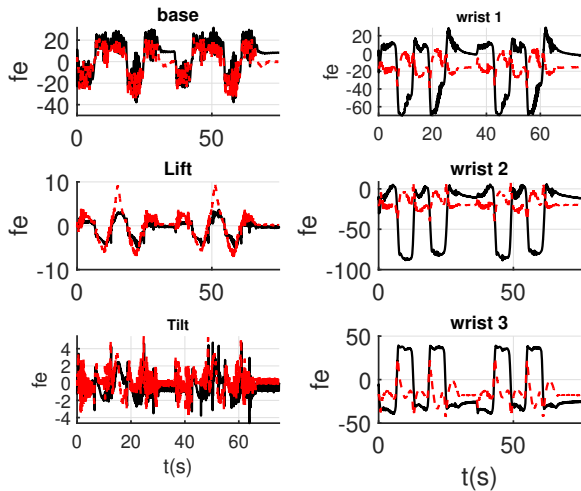


Fig. 13. force errors of each actuator with the implemented controllers. The dashed red line is with RVDC, and the black solid line is with VDC. The y-axis is in kN.

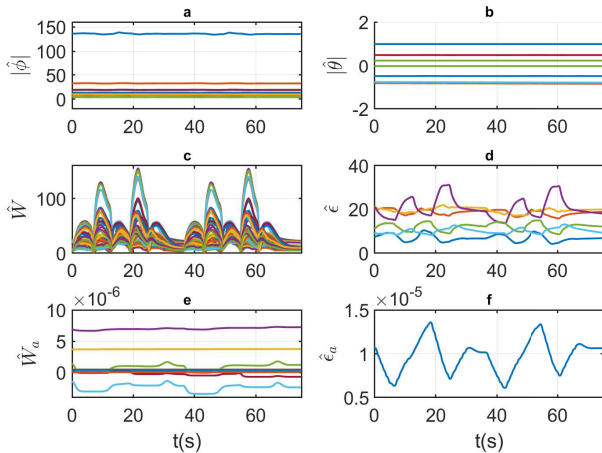


Fig. 14. Time history of estimated parameters. a) norm of estimated inertial parameters, b) estimation of deadzone-backlash parameters, c) time history of updated weights of RBFNNs for the rigid body, d) estimation of bias error, e) weight estimation of RBFNNs for actuators, f) bias error estimation of actuators.

with maximum end-effector velocities of 0.35 m/s , 0.43 m/s , and 0.55 m/s in x , y , and z directions, respectively. The steady-state error in the z -direction with VDC is 14 mm because the motion in the z -direction is mostly generated by the base joint, which is suffering from backlash. Considering the backlash in our proposed method, the steady-state error in the z -direction is reduced to 3 mm . The maximum value of the Cartesian space motion error e_T , demonstrated in Fig. 15, with VDC, is 3 cm , and with the proposed method is 0.9 cm , with the maximum Cartesian velocity of 0.62 m/s . Therefore, the performance index in (1) for VDC and the proposed method is 0.048 and 0.015 , respectively. It can also be seen from Fig. 15 that by tackling the backlash and model uncertainties in the wrist, the proposed method achieved a much better orientation error. Maximum value of orientation error e_{oT} with VDC and the proposed method is 1.78 and 0.55 degrees, respectively. All

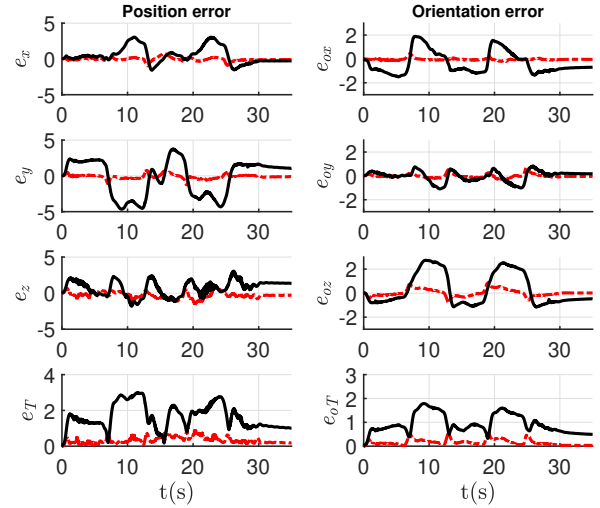


Fig. 15. Position and orientation tracking error of the end-effector in the $x - y - z$ plane. The solid black line is the tracking error with VDC and the dashed red line is with RVDC. The position and orientation errors are presented in cm and deg , respectively.

these results demonstrate a significant improvement in tracking performance.

Finally, experimental results are juxtaposed to those reported in [5], utilizing ρ value as a metric for comparative assessment. Table IV exhibits the computed performance index value for works in which the high-DoF model of HMM is considered. As can be seen, the proposed method has achieved a better ρ value in comparison to other works, demonstrating its excellent behavior in Cartesian space motion control.

Considering all the experimental results provided in this section, along with the comparison to the original VDC approach, the validity of the theoretical results is verified. As shown, tackling unknown model and actuator uncertainties with RBFNNs and handling compound input constraints with an adaptive deadzone-backlash controller significantly improved the tracking performance, both in transient and steady-state. As it was mathematically proved in Theorem 3 and experimentally shown in this section, the designed controller ensured SGUUB stability for the system and converged the tracking error to a substantially small neighborhood of origin.

TABLE IV
PERFORMANCE INDEX EVALUATION OF CARTESIAN SPACE

Study	ρ	DoF	ρ/DoF
This study	0.015	6	0.0025
Kalmari 2015	0.12	4	0.03
Nguyen 2010	0.32	4	0.08
Zhu 2005	0.015	5	0.003
Tsukamoto 2002	0.126	6	0.021
Egelan 1987	0.038	8	0.0047

VIII. CONCLUSION

In this study, an orchestrated robust controller is designed to achieve a precise and robust performance. For this purpose, VDC was employed as the baseline controller. VDC

decomposes the entire complex system into subsystems of the rigid body and actuators by means of VCP. Then, the controller design and stability analysis are accomplished at the subsystem level and expanded to the entire system by means of VPFs and virtual stability. A novel way of incorporating RBFNNs and adaptive inverse deadzone-backlash controllers into each subsystem resulted in the orchestrated robust controller approach. Considering all unknown model and actuator uncertainties, compound input constraints, and unknown disturbances, the SGUUB stability is achieved for the first time in the context of VDC. All theoretical results are validated via extensive simulation and experimental results concerning the highly nonlinear, six DoF heavy-duty hydraulic manipulator. The simulation results demonstrated that the proposed controller outperformed the original VDC, PD, and the state-of-the-art method in the presence of compound input constraints. Moreover, the experimental results demonstrate that the proposed method tackles unknown model and actuator uncertainties and reduces the impact of compound input constraints in real-world applications, resulting in considerably lower transient and steady-state tracking errors and lower actuator force errors in comparison to the original VDC for a given power. Additionally, the proposed method ended up with a precise tracking performance in Cartesian space in comparison to the original VDC. All the analyses, including sensitivity to control gain, tracking performance in joint space and Cartesian space, comparison to the state-of-the-art controller, performance evaluation in the sense of ρ value, and implementation on the real-world six DoF commercial manipulator, display the universality of the proposed method in practical applications.

APPENDIX

A. Proof of Theorem 1

Subtracting (67) from (31) and recalling (66), we have:

$$\begin{aligned} {}^A F_r^* - {}^A F^* &= M_A \frac{d}{dt} ({}^A V_r - {}^A V) + C_A ({}^A \omega) ({}^A V_r - {}^A V) \\ &\quad + K_A ({}^A V_r - {}^A V) + Y_A \tilde{\phi}_A + {}^A \tilde{W}^T \Psi(\chi_A) + {}^A \tilde{\varepsilon}. \end{aligned} \quad (116)$$

Now, by defining the non-negative accompanying function in the sense of Definition 3 as:

$$\begin{aligned} \nu_1 &= \sum_{A \in S} \frac{1}{2} ({}^A V_r - {}^A V)^T M_A ({}^A V_r - {}^A V) \\ &\quad + \sum_{A \in S} \gamma \mathcal{D}_F(\mathcal{L}_A \| \hat{\mathcal{L}}_A) + \frac{1}{2} \text{tr}({}^A \tilde{W}^T A \Gamma^{-1} A \tilde{W}) \quad (117) \\ &\quad + \frac{1}{2} {}^A \tilde{\varepsilon}^T A \tilde{\varepsilon}. \end{aligned}$$

where $\mathcal{D}_F(\mathcal{L}_A \| \hat{\mathcal{L}}_A)$ is in the sense of Lemma 3, ${}^A \Gamma \in \mathbb{R}^{\tilde{n}_A \times \tilde{n}_A}$ is a positive-definite matrix, and ${}^A \pi \in \mathbb{R}$ is a positive constant gain. Consider $\mathcal{D}_F(\mathcal{L}_A \| \hat{\mathcal{L}}_A) \leq \text{tr}(\tilde{\mathcal{L}}_A \tilde{\mathcal{L}}_A)$ With $\|\tilde{\mathcal{L}}_A\|_F^2 = \text{tr}(\tilde{\mathcal{L}}_A \tilde{\mathcal{L}}_A)$, where $\|\cdot\|_F$ is the Frobenius norm of a matrix. It can be shown for ν_1 that:

$$\begin{aligned} \nu_1 &\leq \mu_1 \left(\sum_{A \in S} ({}^A V_r - {}^A V)^T ({}^A V_r - {}^A V) \right. \\ &\quad \left. + \text{tr}({}^A \tilde{W}^T A \tilde{W}) + {}^A \tilde{\varepsilon}^T A \tilde{\varepsilon} \right) \end{aligned} \quad (118)$$

with $\mu_1 = \max \{ \gamma, \{ \lambda_{\max}(M), 0.5(\lambda_{\max}(\Gamma)), 0.5{}^A \pi^{-1} \}_{A \in S} \}$, where $\lambda_{\max}(\cdot)$ is the maximum eigenvalue of the matrix. Taking the time derivative of (117) with using (116), defining ${}^A S = {}^A Y^T ({}^A V_r - {}^A V)$, and ${}^A \tilde{\phi}^T {}^A S = \text{tr}({}^A \tilde{\mathcal{L}}^T {}^A S)$, exploiting $({}^A V_r - {}^A V)^T {}^A \tilde{W}^T \Psi(\chi_A) = \text{tr}(({}^A V_r - {}^A V) \Psi^T(\chi_A) {}^A \tilde{W})$, and replacing from (105)-(107), one can achieve:

$$\begin{aligned} \dot{\nu}_1 &= \sum_{A \in S} ({}^A V_r - {}^A V)^T ({}^A F_r^* - {}^A F^*) \\ &\quad - ({}^A V_r - {}^A V)^T K_A ({}^A V_r - {}^A V) \\ &\quad - \gamma_0 \text{tr}(\hat{\mathcal{L}}_A \tilde{\mathcal{L}}_A) - {}^A \tau_0 \text{tr}({}^A \tilde{W}^T A \tilde{W}) - {}^A \pi_0 {}^A \tilde{\varepsilon}^T A \tilde{\varepsilon}. \end{aligned} \quad (119)$$

The first term in (119) is the VPF of the corresponding frame $\{A\}$. In order to expand the VPFs, we need to use the Definition 2 for each frame in $\{S\}$. Starting from $\{P_1\}$ and recalling (3), (46), and (73), we have:

$$\begin{aligned} \dot{\nu}_{P_1} &= ({}^{P_1} V_r - {}^{P_1} V)^T ({}^{P_1} F_r^* - {}^{P_1} F^*) \\ &= ({}^{P_1} V_r - {}^{P_1} V)^T ({}^{P_1} F_r - {}^{P_1} F) \\ &\quad + ({}^{P_1} V_r - {}^{P_1} V)^T {}^{P_1} U_{B_{c1}} ({}^{B_{c1}} F_r - {}^{B_{c1}} F) \\ &= p_{P_1} - ({}^{P_1} U_{B_{c1}}^T ({}^{P_1} V_r - {}^{P_1} V))^T ({}^{B_{c1}} F_r - {}^{B_{c1}} F) \\ &= p_{P_1} - ({}^{B_{c1}} V_r - {}^{B_{c1}} V)^T ({}^{B_{c1}} F_r - {}^{B_{c1}} F) \end{aligned} \quad (120)$$

By replacing from (72) and (41) for $j = 1$ and taking the same procedure in (120), we have:

$$\begin{aligned} \dot{\nu}_{P_1} &= p_{P_1} - ({}^{B_{c1}} V_r - {}^{B_{c1}} V)^T ({}^{B_{01}} F_r - {}^{B_{01}} F) \\ &\quad + ({}^{B_{c1}} V_r - {}^{B_{c1}} V)^T {}^{B_{01}} U_{B_{11}} ({}^{B_{11}} F_r - {}^{B_{11}} F) \\ &\quad - ({}^{B_{c1}} V_r - {}^{B_{c1}} V)^T {}^{B_{01}} U_{B_{11}} ({}^{B_{11}} F_r - {}^{B_{11}} F) \\ &\quad + ({}^{B_{c1}} V_r - {}^{B_{c1}} V)^T {}^{B_{01}} U_{B_{c2}} ({}^{B_{c2}} F_r - {}^{B_{c2}} F) \\ &\quad - ({}^{B_{c1}} V_r - {}^{B_{c1}} V)^T {}^{B_{01}} U_{P_{11}} ({}^{P_{11}} F_r - {}^{P_{11}} F) \\ &\quad - ({}^{B_{c1}} V_r - {}^{B_{c1}} V)^T {}^{B_{21}} U_{B_{31}} ({}^{B_{31}} F_r - {}^{B_{31}} F) \\ &\quad + ({}^{B_{c1}} V_r - {}^{B_{c1}} V)^T {}^{B_{21}} U_{B_{41}} ({}^{B_{41}} F_r - {}^{B_{41}} F) \\ &\quad - ({}^{B_{c1}} V_r - {}^{B_{c1}} V)^T {}^{B_{21}} U_{B_{41}} ({}^{B_{41}} F_r - {}^{B_{41}} F) \\ &\quad + ({}^{B_{c1}} V_r - {}^{B_{c1}} V)^T {}^{B_{21}} U_{P_{11}} ({}^{P_{11}} F_r - {}^{P_{11}} F) \\ &\quad - ({}^{B_{c1}} V_r - {}^{B_{c1}} V)^T {}^{B_{01}} U_{B_{c2}} ({}^{B_{c2}} F_r - {}^{B_{c2}} F) \\ &= p_{P_1} - p_{B_{01}} + p_{B_{11}} - p_{B_{11}} + p_{B_{c2}} - p_{P_{11}} \\ &\quad - p_{B_{21}} + p_{B_{41}} - p_{B_{41}} + p_{P_{11}} - p_{B_{c2}} \\ &= p_{P_1} - p_{B_{01}} - p_{B_{21}}. \end{aligned} \quad (121)$$

In the same sense, we can write for all other frames in $\{S\}$:

$$\dot{\nu}_{P_{p2}} = p_{P_{p2}} \quad (122)$$

$$\dot{\nu}_{B_{0j}} = p_{B_{0j}} - p_{B_{1j}} \quad (123)$$

$$\dot{\nu}_{B_{1j}} = p_{B_{1j}} - p_{B_{c,j+1}} + p_{P_{1j}} \quad (124)$$

$$\dot{\nu}_{B_{3j}} = p_{B_{2j}} - p_{B_{4j}} + (f_{cjr} - f_{cj})(\dot{x}_{pjr} - \dot{x}_{pj}) \quad (125)$$

$$\dot{\nu}_{B_{4j}} = p_{B_{4j}} - p_{P_{1j}} \quad (126)$$

$$\dot{\nu}_{G_i} = p_{G_i} - p_{E_{i+1}}. \quad (127)$$

On the other hand, in (119), by recalling Lemma 2, using Trace operator property and the fact that $\hat{\mathcal{L}}_A$ is a positive-definite and symmetric matrix along with $\hat{\mathcal{L}}_A = \tilde{\mathcal{L}}_A + \mathcal{L}_A$, we have: $-\text{tr}(\hat{\mathcal{L}}_A \tilde{\mathcal{L}}_A) = -\text{tr}(\tilde{\mathcal{L}}_A \tilde{\mathcal{L}}_A) - \text{tr}(\mathcal{L}_A \tilde{\mathcal{L}}_A)$. Additionally, it can be shown that $-\text{tr}(\mathcal{L}_A \tilde{\mathcal{L}}_A) \leq 0.5 \left(\text{tr}(\tilde{\mathcal{L}}_A \tilde{\mathcal{L}}_A) + \text{tr}(\mathcal{L}_A \mathcal{L}_A) \right)$. Therefore, we can write that $-\text{tr}(\hat{\mathcal{L}}_A \tilde{\mathcal{L}}_A) \leq -0.5 \text{tr}(\tilde{\mathcal{L}}_A \tilde{\mathcal{L}}_A) + 0.5 \text{tr}(\mathcal{L}_A \mathcal{L}_A)$. In the same way, we can write that $-A_{\tilde{\varepsilon}}^T A_{\tilde{\varepsilon}} \leq -0.5 A_{\tilde{\varepsilon}}^T A_{\tilde{\varepsilon}} + 0.5 A_{\varepsilon}^T A_{\varepsilon}$, and $-\text{tr}(A \tilde{W}^T A \tilde{W}) \leq -0.5 \text{tr}(A \tilde{W}^T A \tilde{W}) + 0.5 \text{tr}(A W^T A W)$. Therefore, by replacing (121)-(127) in (119), and considering $p_{B_{c2}} = p_{B_{02}} + p_{B_{22}}$ and $p_{B_{c3}} = p_{E_1}$ with using (118), we have:

$$\dot{\nu}_1 \leq -\mu \nu_1 + \mu_0 + VPFs \quad (128)$$

where $VPFs = p_{P_1} + p_{P_{p2}} + p_{G_1} + p_{G_2} + p_{G_3} - p_{E_1} - p_{E_2} - p_{E_3} - p_{E_4} + \sum_{j=1,2} (f_{cjr} - f_{cj})(\dot{x}_{pjr} - \dot{x}_{pj})$. Additionally, $\mu = \mu_2 / \mu_1$, where $\mu_2 = \min \{ \gamma_0, \{ \lambda_{\min}(A K), 0.5^A \tau_0, 0.5^A \pi_0^{-1} \}_{A \in S} \}$, and $\mu_0 = \sum_{A \in S} 0.5 \gamma_0 \text{tr}(\mathcal{L}_A \mathcal{L}_A) + 0.5^A \tau_0 \text{tr}(A W^T A W) + 0.5^A \pi_0 A_{\tilde{\varepsilon}}^T A_{\tilde{\varepsilon}}$.

B. Proof of Theorem 2

By subtracting (100) from (96), adding $(\dot{f}_{pr} - \dot{f}_p) / \beta$ to the right side, using (97), (102), and (104), we have:

$$\begin{aligned} \frac{1}{\beta} (\dot{f}_{pr} - \dot{f}_p) &= -Y_d \tilde{\theta}_d - Y_v \tilde{\theta}_v - k_f (f_{pr} - f_p) \\ &\quad - k_x (\dot{x}_{pr} - \dot{x}_p) - \tilde{W}_a^T \Psi(\chi_a) - \tilde{\varepsilon}_a - \tilde{\theta}^T \eta. \end{aligned} \quad (129)$$

Define the non-negative accompanying function as:

$$\begin{aligned} \nu_a &= (f_{ppr} - f_{pp})^2 / (2\beta k_{xp}) + \sum_{j=1,2} (f_{pjr} - f_{pj})^2 / (2\beta k_{xj}) \\ &\quad + \sum_{i=1,2,3} (f_{pwir} - f_{pwi})^2 / (2\beta k_{xwi}) + \frac{1}{2\gamma_{dp}} (\tilde{\theta}_{dp}^T \tilde{\theta}_{dp}) \\ &\quad + \sum_{j=1,2} \frac{1}{2\gamma_{dj}} (\tilde{\theta}_{dj}^T \tilde{\theta}_{dj}) + \sum_{i=1,2,3} \frac{1}{2\gamma_{dwi}} (\tilde{\theta}_{dwi}^T \tilde{\theta}_{dwi}) \\ &\quad + \frac{1}{2\gamma_{vp}} (\tilde{\theta}_{vp}^T \tilde{\theta}_{vp}) + \sum_{j=1,2} \frac{1}{2\gamma_{vj}} (\tilde{\theta}_{vj}^T \tilde{\theta}_{vj}) \\ &\quad + \sum_{i=1,2,3} \frac{1}{2\gamma_{vwi}} (\tilde{\theta}_{vwi}^T \tilde{\theta}_{vwi}) + \sum_{j=1,2} \frac{1}{2\gamma_{fj}} (\tilde{\theta}_{fj}^T \tilde{\theta}_{fj}) \\ &\quad + \frac{1}{2\gamma_{fp}} (\tilde{\theta}_{fp}^T \tilde{\theta}_{fp}) + \sum_{i=1,2,3} \frac{1}{2\gamma_{fwi}} (\tilde{\theta}_{fwi}^T \tilde{\theta}_{fwi}) \\ &\quad + \frac{1}{2\delta_p} (\tilde{W}_{ap}^T \tilde{W}_{ap}) + \sum_{j=1,2} \frac{1}{2\delta_j} (\tilde{W}_{aj}^T \tilde{W}_{aj}) \\ &\quad + \sum_{i=1,2,3} \frac{1}{2\delta_{wi}} (\tilde{W}_{awi}^T \tilde{W}_{awi}) + \sum_{i=1,2,3} \frac{1}{2\delta_{wi}} (\tilde{\varepsilon}_{awi})^2 \\ &\quad + \frac{1}{2\delta_p} (\tilde{\varepsilon}_{ap})^2 + \sum_{j=1,2} \frac{1}{2\delta_j} (\tilde{\varepsilon}_{aj})^2 + \frac{1}{2\delta_{p\theta}} (\tilde{\theta}_p^T \tilde{\theta}_p) \\ &\quad + \sum_{j=1,2} \frac{1}{2\delta_{j\theta}} (\tilde{\theta}_j^T \tilde{\theta}_j) + \sum_{i=1,2,3} \frac{1}{2\delta_{wi\theta}} (\tilde{\theta}_{awi}^T \tilde{\theta}_{awi}) \end{aligned} \quad (130)$$

with $k_{x(\cdot)}$ being a positive constant. By computing (129) for each linear hydraulic actuator, choosing the adaptation functions as in (109)- (114), (99), (87), and (86), and substituting in the time derivative of (130), we have:

$$\begin{aligned} \dot{\nu}_a &= -\frac{k_{fp}}{k_{xp}} (f_{ppr} - f_{pp})^2 - \sum_{j=1,2} \frac{k_{fj}}{k_{xj}} (f_{pjr} - f_{pj})^2 \\ &\quad - \sum_{i=1,2,3} \frac{k_{fwi}}{k_{xwi}} (f_{pwir} - f_{pwi})^2 \\ &\quad - (f_{cpr} - f_{cp})(\dot{x}_{ppr} - \dot{x}_{pp}) - \sum_{j=1,2} (f_{cjr} - f_{cj})(\dot{x}_{pjr} - \dot{x}_{pj}) \\ &\quad - \sum_{i=1,2,3} (f_{cwir} - f_{cwi})(\dot{x}_{pwir} - \dot{x}_{pwi}) \\ &\quad - \gamma_{dp0} \tilde{\theta}_{dp}^T \hat{\theta}_{dp} - \sum_{j=1,2} \gamma_{dj0} \tilde{\theta}_{dj}^T \hat{\theta}_{dj} - \sum_{i=1,2,3} \gamma_{dwi0} \tilde{\theta}_{dwi}^T \hat{\theta}_{dwi} \\ &\quad - \gamma_{vp0} \tilde{\theta}_{vp}^T \hat{\theta}_{vp} - \sum_{j=1,2} \gamma_{vj0} \tilde{\theta}_{vj}^T \hat{\theta}_{vj} \\ &\quad - \sum_{i=1,2,3} \gamma_{vwi0} \tilde{\theta}_{vwi}^T \hat{\theta}_{vwi} - \gamma_{fp0} \tilde{\theta}_{fp}^T \hat{\theta}_{fp} - \sum_{j=1,2} \gamma_{fj0} \tilde{\theta}_{fj}^T \hat{\theta}_{fj} \\ &\quad - \sum_{i=1,2,3} \gamma_{fwi0} \tilde{\theta}_{fwi}^T \hat{\theta}_{fwi} \\ &\quad - \delta_{p0} \tilde{W}_{ap}^T \hat{W}_{ap} - \sum_{j=1,2} \delta_{j0} \tilde{W}_{aj}^T \hat{W}_{aj} - \sum_{i=1,2,3} \delta_{wi0} \tilde{W}_{awi}^T \hat{W}_{awi} \\ &\quad - \bar{\delta}_{p0} \tilde{\varepsilon}_{ap} \hat{\varepsilon}_{ap} - \sum_{j=1,2} \bar{\delta}_{j0} \tilde{\varepsilon}_{aj} \hat{\varepsilon}_{aj} \\ &\quad - \sum_{i=1,2,3} \bar{\delta}_{wi0} \tilde{\varepsilon}_{awi} \hat{\varepsilon}_{awi} - \delta_{p\theta0} \tilde{\theta}_p^T \hat{\theta}_p - \sum_{j=1,2} \delta_{j\theta0} \tilde{\theta}_j^T \hat{\theta}_j \\ &\quad - \sum_{i=1,2,3} \delta_{wi\theta0} \tilde{\theta}_{wi}^T \hat{\theta}_{wi} \end{aligned} \quad (131)$$

By considering (10), (53), and (76), one can rewrite the VPFs in (131) as:

$$\begin{aligned} \dot{\nu}_{aP_1} &= -(\dot{x}_{ppr} - \dot{x}_{pp})(f_{cpr} - f_{cp}) \\ &= -\left(\frac{1}{r_p} y_r (\dot{x}_{ppr} - \dot{x}_{pp}) \right)^T (P_1 F_r - P_1 F) \\ &\quad - (x_f (\dot{x}_{ppr} - \dot{x}_{pp}))^T (P_{p2} F_r - P_{p2} F) \\ &= - (P_1 V_r - P_1 V)^T (P_1 F_r - P_1 F) \\ &\quad - (P_{p2} V_r - P_{p2} V)^T (P_{p2} F_r - P_{p2} F) \\ &\quad + (P_{p1} U_{P_{p2}}^T (P_{p1} V_r - P_{p1} V))^T (P_{p1} F_r - P_{p1} F) \\ &= -p_{P_1} - p_{P_{p2}} + p_{P_{p1}} \end{aligned} \quad (132)$$

and,

$$\dot{\nu}_{aG_i} = -(f_{cwir} - f_{cwi})(\dot{x}_{pwir} - \dot{x}_{pwi}) = -p_{G_i} + p_{E_i}. \quad (133)$$

On the other hand, we know $\hat{\theta}_{(\varepsilon)} = \tilde{\theta}_{(\varepsilon)} + \theta_{(\varepsilon)}$. Then we can write $-\tilde{\theta}_{(\varepsilon)}^T \hat{\theta}_{(\varepsilon)} = -\tilde{\theta}_{(\varepsilon)}^T \tilde{\theta}_{(\varepsilon)} - \tilde{\theta}_{(\varepsilon)}^T \theta_{(\varepsilon)}$. Moreover, $-\tilde{\theta}_{(\varepsilon)}^T \theta_{(\varepsilon)} \leq 0.5 \left(\tilde{\theta}_{(\varepsilon)}^T \tilde{\theta}_{(\varepsilon)} + \theta_{(\varepsilon)}^T \theta_{(\varepsilon)} \right)$. Therefore, we have $-\tilde{\theta}_{(\varepsilon)}^T \hat{\theta}_{(\varepsilon)} \leq -0.5 \tilde{\theta}_{(\varepsilon)}^T \tilde{\theta}_{(\varepsilon)} + 0.5 \theta_{(\varepsilon)}^T \theta_{(\varepsilon)}$. By doing the same for

all the same terms in (131) and substituting (132) and (133), one can obtain:

$$\begin{aligned}
\dot{\nu}_a \leq & -\frac{k_{fp}}{k_{xp}}(f_{ppr} - f_{pp})^2 - \sum_{j=1,2} \frac{k_{fj}}{k_{xj}}(f_{pjr} - f_{pj})^2 \\
& - \sum_{i=1,2,3} \frac{k_{fwi}}{k_{xwi}}(f_{pwir} - f_{pwi})^2 + VPFs \\
& - 0.5\gamma_{dp0}\tilde{\theta}_{dp}^T\tilde{\theta}_{dp} - 0.5\sum_{j=1,2} \gamma_{dj0}\tilde{\theta}_{dj}^T\tilde{\theta}_{dj} \\
& - 0.5\sum_{i=1,2,3} \gamma_{dwi0}\tilde{\theta}_{dwi}^T\tilde{\theta}_{dwi} - 0.5\gamma_{vp0}\tilde{\theta}_{vp}^T\tilde{\theta}_{vp} \\
& - 0.5\sum_{j=1,2} \gamma_{vj0}\tilde{\theta}_{vj}^T\tilde{\theta}_{vj} - 0.5\sum_{i=1,2,3} \gamma_{vwi0}\tilde{\theta}_{vwi}^T\tilde{\theta}_{vwi} \\
& - 0.5\gamma_{fp0}\tilde{\theta}_{fp}^T\tilde{\theta}_{fp} - 0.5\sum_{i=1,2,3} \gamma_{fwi0}\tilde{\theta}_{fwi}^T\tilde{\theta}_{fwi} \\
& - 0.5\sum_{j=1,2} \gamma_{fj0}\tilde{\theta}_{fj}^T\tilde{\theta}_{fj} - 0.5\sum_{i=1,2,3} \delta_{wi0}\tilde{W}_{awi}^T\tilde{W}_{awi} \\
& - 0.5\delta_{p0}\tilde{W}_{ap}^T\tilde{W}_{ap} - 0.5\sum_{j=1,2} \delta_{j0}\tilde{W}_{aj}^T\tilde{W}_{aj} \\
& - 0.5\bar{\delta}_{p0}\tilde{\varepsilon}_{ap}\tilde{\varepsilon}_{ap} - 0.5\sum_{j=1,2} \bar{\delta}_{j0}\tilde{\varepsilon}_{aj}\tilde{\varepsilon}_{aj} \\
& - 0.5\sum_{i=1,2,3} \bar{\delta}_{wi0}\tilde{\varepsilon}_{awi}\tilde{\varepsilon}_{awi} - 0.5\delta_{p\theta0}\tilde{\theta}_p^T\tilde{\theta}_p \\
& - 0.5\sum_{j=1,2} \delta_{j\theta0}\tilde{\theta}_j^T\tilde{\theta}_j - 0.5\sum_{i=1,2,3} \delta_{wi\theta0}\tilde{\theta}_{wi}^T\tilde{\theta}_{wi} \\
& + 0.5\gamma_{dp0}\theta_{dp}^T\theta_{dp} + 0.5\sum_{j=1,2} \gamma_{dj0}\theta_{dj}^T\theta_{dj} \\
& + 0.5\sum_{i=1,2,3} \gamma_{dwi0}\theta_{dwi}^T\theta_{dwi} + 0.5\gamma_{vp0}\theta_{vp}^T\theta_{vp} \\
& + 0.5\sum_{j=1,2} \gamma_{vj0}\theta_{vj}^T\theta_{vj} + 0.5\sum_{j=1,2} \bar{\delta}_{j0}\varepsilon_{aj}\varepsilon_{aj} \\
& + 0.5\sum_{i=1,2,3} \gamma_{vwi0}\theta_{vwi}^T\theta_{vwi} + 0.5\gamma_{fp0}\theta_{fp}^T\theta_{fp} \\
& + 0.5\sum_{j=1,2} \gamma_{fj0}\theta_{fj}^T\theta_{fj} + 0.5\sum_{i=1,2,3} \gamma_{fwi0}\theta_{fwi}^T\theta_{fwi} \\
& + 0.5\delta_{p0}W_{ap}^T W_{ap} + 0.5\sum_{j=1,2} \delta_{j0}W_{aj}^T W_{aj} \\
& + 0.5\sum_{i=1,2,3} \delta_{wi0}W_{awi}^T W_{awi} + 0.5\bar{\delta}_{p0}\varepsilon_{ap}\varepsilon_{ap} \\
& + 0.5\sum_{i=1,2,3} \bar{\delta}_{wi0}\varepsilon_{awi}\varepsilon_{awi} + 0.5\delta_{p\theta0}\theta_p^T\theta_p \\
& + 0.5\sum_{j=1,2} \delta_{j\theta0}\theta_j^T\theta_j + 0.5\sum_{i=1,2,3} \delta_{wi\theta0}\theta_{wi}^T\theta_{wi} \\
\leq & -\mu_a\nu_{a2} + \mu_{a0} + VPFs.
\end{aligned} \tag{134}$$

where $VPFs = -p_{P_1} - p_{P_2} + p_{P_1} - \sum_{j=1,2}(f_{cjr} - f_{cj})(\dot{x}_{pjr} - \dot{x}_{pj}) + \sum_{i=1,2,3}(-p_{G_i} + p_{E_i})$. In the same sense in (118) and (128) we have $\mu_a = \mu_{1a}/\mu_{2a}$, where $\mu_{1a} = \min(\frac{k_{fp}}{k_{xp}}, \frac{k_{fj}}{k_{xj}}, \frac{k_{fwi}}{k_{xwi}}, 0.5\gamma_{dp0}, 0.5\gamma_{dj0}, 0.5\gamma_{dwi0}, 0.5\gamma_{vp0}, 0.5\gamma_{vj0}, 0.5\gamma_{vwi0}, 0.5\gamma_{fp0}, 0.5\gamma_{fj0}, 0.5\gamma_{fwi0}, 0.5\delta_{p0}, 0.5\delta_{j0}, 0.5\delta_{wi0}, 0.5\bar{\delta}_{p0}, 0.5\bar{\delta}_{j0}, 0.5\bar{\delta}_{wi0}, 0.5\delta_{p\theta0}, 0.5\delta_{j\theta0}, 0.5\delta_{wi\theta0})$,

while $\mu_{2a} = \max(\frac{1}{2\beta k_{xp}}, \frac{1}{2\beta k_{xj}}, \frac{1}{2\beta k_{xwi}}, \frac{1}{2\gamma_{dp}}, \frac{1}{2\gamma_{dj}}, \frac{1}{2\gamma_{dwi}}, \frac{1}{2\gamma_{vp}}, \frac{1}{2\gamma_{vj}}, \frac{1}{2\gamma_{vwi}}, \frac{1}{2\gamma_{fp}}, \frac{1}{2\gamma_{fj}}, \frac{1}{2\gamma_{fwi}}, \frac{1}{2\delta_p}, \frac{1}{2\delta_j}, \frac{1}{2\delta_{wi}}, \frac{1}{2\bar{\delta}_p}, \frac{1}{2\bar{\delta}_j}, \frac{1}{2\bar{\delta}_{wi}})$, and $\mu_{a0} = (0.5\gamma_{dp0}\theta_{dp}^T\theta_{dp} + 0.5\sum_{j=1,2} \gamma_{dj0}\theta_{dj}^T\theta_{dj} + 0.5\sum_{i=1,2,3} \gamma_{dwi0}\theta_{dwi}^T\theta_{dwi} + 0.5\gamma_{vp0}\theta_{vp}^T\theta_{vp} + 0.5\sum_{j=1,2} \gamma_{vj0}\theta_{vj}^T\theta_{vj} + 0.5\sum_{i=1,2,3} \gamma_{vwi0}\theta_{vwi}^T\theta_{vwi} + 0.5\gamma_{fp0}\theta_{fp}^T\theta_{fp} + 0.5\sum_{j=1,2} \gamma_{fj0}\theta_{fj}^T\theta_{fj} + 0.5\sum_{i=1,2,3} \gamma_{fwi0}\theta_{fwi}^T\theta_{fwi}) + 0.5\delta_{p0}W_{ap}^T W_{ap} + 0.5\sum_{j=1,2} \delta_{j0}W_{aj}^T W_{aj} + 0.5\sum_{i=1,2,3} \delta_{wi0}W_{awi}^T W_{awi} + 0.5\bar{\delta}_{p0}\varepsilon_{ap}\varepsilon_{ap} + ap + 0.5\sum_{j=1,2} \delta_{j0}\varepsilon_{aj}\varepsilon_{aj} + 0.5\sum_{i=1,2,3} \bar{\delta}_{wi0}\varepsilon_{awi}\varepsilon_{awi} + 0.5\delta_{p\theta0}\theta_p^T\theta_p + 0.5\sum_{j=1,2} \delta_{j\theta0}\theta_j^T\theta_j + 0.5\sum_{i=1,2,3} \delta_{wi\theta0}\theta_{wi}^T\theta_{wi}$.

C. Proof of Theorem 3

Define the non-negative accompanying function as below:

$$\nu = \nu_1 + \nu_a \tag{135}$$

Taking the time derivative of (135), one can obtain:

$$\begin{aligned}
\dot{\nu} \leq & -\mu\nu_1 + \mu_0 + p_{P_1} + p_{P_2} + p_{G_1} + p_{G_2} + p_{G_3} \\
& - p_{E_1} - p_{E_2} - p_{E_3} - p_{E_4} + \sum_{j=1,2} (f_{cjr} - f_{cj})(\dot{x}_{pjr} - \dot{x}_{pj}) \\
& - \mu_a\nu_a + \mu_{a0} - p_{P_1} - p_{P_2} + p_{E_1} + p_{E_2} + p_{E_3} \\
& - \sum_{j=1,2} (f_{cjr} - f_{cj})(\dot{x}_{pjr} - \dot{x}_{pj}) - p_{G_1} - p_{G_2} - p_{G_3} \\
\leq & -\bar{\mu}\nu + \bar{\mu}_0 + p_{P_1} - p_{E_4}
\end{aligned} \tag{136}$$

with $\bar{\mu} = (\min\{\mu, \mu_a\}) / (\max\{\mu_1, \mu_{2a}\})$ and $\bar{\mu}_0 = \mu_0 + \mu_{a0}$ being positive. Moreover, since there is no contact with the environment and the base is fixed, $p_{E_4} = p_{P_1} = 0$. Now, multiplying both sides by $e^{\bar{\mu}t}$, (136) becomes:

$$\frac{d}{dt}(\nu(t)e^{\bar{\mu}t}) \leq \bar{\mu}_0 e^{\bar{\mu}t}. \tag{137}$$

Integrating (137) over $[0, t]$, one can obtain:

$$\nu(t) \leq \nu(0)e^{-\bar{\mu}t} + \frac{\bar{\mu}_0}{\bar{\mu}}(1 - e^{-\bar{\mu}t}) \leq \nu(0) + \frac{\bar{\mu}_0}{\bar{\mu}}. \tag{138}$$

Considering (117) and (135), we can derive for the velocity error $\frac{1}{2}(A^T V_r - A^T V)^T M_A (A^T V_r - A^T V) \leq \nu(t) \leq \nu(0) + \frac{\bar{\mu}_0}{\bar{\mu}}$

which results in $\|(A^T V_r - A^T V)\| \leq \sqrt{2\frac{\nu(0) + \frac{\bar{\mu}_0}{\bar{\mu}}}{\lambda_{\min}(M)}}$. Therefore, it

can be concluded that $\lim_{t \rightarrow \infty} \|(A^T V_r - A^T V)\| = \sqrt{\frac{2\bar{\mu}_0}{\bar{\mu}\lambda_{\min}(M)}}$.

It can be seen that by fine-tuning the control gains in $\bar{\mu}$, the compact set can be very small near zero. In the same

way, we can achieve $\lim_{t \rightarrow \infty} \|(f_{p(\cdot)r} - f_{p(\cdot)})\| \leq \sqrt{\frac{2\beta k_{x(\cdot)}\bar{\mu}_0}{\bar{\mu}}}$

(with (\cdot) indicating all joints), which ensures the semi-global boundedness of the force tracking error in the presence of all the uncertainties. We can derive the same conclusion for the update law of the RBFNNs weights as $\lim_{t \rightarrow \infty} \|\tilde{W}_a(\cdot)\| \leq \sqrt{\frac{2\delta(\cdot)\bar{\mu}_0}{\bar{\mu}}}$. For all other errors, the compact set can be achieved as well.

REFERENCES

- [1] ABB, "8th generation of heavy payload robot," [Online]. Available: <https://search.abb.com/library/Download.aspx?DocumentID=3HAC052852-001&LanguageCode=en&DocumentPartId=&Action=Launch>, accessed: November 29, 2023.
- [2] S. MineStories, "The automine journey," [Online]. Available: <https://minestories.com/automine-journey/>, accessed: September 27, 2023.
- [3] K. Gribbins, "The ultimate mini ex overview: A comprehensive analysis of the 2021 compact excavator market," [Online]. Available: <https://compactequip.com/excavators/the-ultimate-mini-ex-overview-a-comprehensive-analysis-of-the-2021-compact-excavator-market/>, accessed: September 27, 2023.
- [4] K. S. Saidi, T. Bock, and C. Georgoulas, "Robotics in construction," in *Springer handbook of robotics*. Springer, 2016, pp. 1493–1520.
- [5] J. Mattila, J. Koivumäki, D. G. Caldwell, and C. Semini, "A survey on control of hydraulic robotic manipulators with projection to future trends," *iEeE/ASME Transactions on Mechatronics*, vol. 22, no. 2, pp. 669–680, 2017.
- [6] G. R. Petrović and J. Mattila, "Mathematical modelling and virtual decomposition control of heavy-duty parallel–serial hydraulic manipulators," *Mechanism and Machine Theory*, vol. 170, p. 104680, 2022.
- [7] A. Bonchis, P. I. Corke, and D. C. Rye, "Experimental evaluation of position control methods for hydraulic systems," *IEEE Transactions on Control Systems Technology*, vol. 10, no. 6, pp. 876–882, 2002.
- [8] M. M. Bech, T. O. Andersen, H. C. Pedersen, and L. Schmidt, "Experimental evaluation of control strategies for hydraulic servo robot," in *2013 IEEE International Conference on Mechatronics and Automation*. IEEE, 2013, pp. 342–347.
- [9] F. Bu and B. Yao, "Observer based coordinated adaptive robust control of robot manipulators driven by single-rod hydraulic actuators," in *Proceedings 2000 ICRA. Millennium Conference. IEEE International Conference on Robotics and Automation. Symposia Proceedings (Cat. No. 00CH37065)*, vol. 3. IEEE, 2000, pp. 3034–3039.
- [10] F. Bu and B. Yuo, "Desired compensation adaptive robust control of single-rod electro-hydraulic actuator," in *Proceedings of the 2001 American Control Conference (Cat. No. 01CH37148)*, vol. 5. IEEE, 2001, pp. 3926–3931.
- [11] W.-H. Zhu and J.-C. Piedboeuf, "Adaptive output force tracking control of hydraulic cylinders with applications to robot manipulators," *Journal of Dynamic Systems, Measurement, and Control*, vol. 127, no. 2, pp. 206–217, 2005.
- [12] W.-H. Zhu, *Virtual decomposition control: toward hyper degrees of freedom robots*. Springer Science & Business Media, 2010, vol. 60.
- [13] J. Koivumäki and J. Mattila, "The automation of multi degree of freedom hydraulic crane by using virtual decomposition control," in *2013 IEEE/ASME International Conference on Advanced Intelligent Mechatronics*. IEEE, 2013, pp. 912–919.
- [14] J. Koivumäki, W.-H. Zhu, and J. Mattila, "Energy-efficient and high-precision control of hydraulic robots," *Control Engineering Practice*, vol. 85, pp. 176–193, 2019.
- [15] X. Liang, Z. Yao, W. Deng, and J. Yao, "Adaptive control of n-link hydraulic manipulators with gravity and friction identification," *Nonlinear Dynamics*, pp. 1–17, 2023.
- [16] X. Yang, W. Deng, and J. Yao, "Neural adaptive dynamic surface asymptotic tracking control of hydraulic manipulators with guaranteed transient performance," *IEEE Transactions on Neural Networks and Learning Systems*, 2022.
- [17] J. Kim, M. Jin, W. Choi, and J. Lee, "Discrete time delay control for hydraulic excavator motion control with terminal sliding mode control," *Mechatronics*, vol. 60, pp. 15–25, 2019.
- [18] W. Deng, H. Zhou, J. Zhou, and J. Yao, "Neural network-based adaptive asymptotic prescribed performance tracking control of hydraulic manipulators," *IEEE transactions on systems, man, and cybernetics: systems*, vol. 53, no. 1, pp. 285–295, 2022.
- [19] S. Lampinen, J. Koivumäki, W.-H. Zhu, and J. Mattila, "Force-sensorless bilateral teleoperation control of dissimilar master–slave system with arbitrary scaling," *IEEE Transactions on Control Systems Technology*, vol. 30, no. 3, pp. 1037–1051, 2021.
- [20] J. Koivumäki and J. Mattila, "Stability-guaranteed force-sensorless contact force/motion control of heavy-duty hydraulic manipulators," *IEEE Transactions on Robotics*, vol. 31, no. 4, pp. 918–935, 2015.
- [21] M. Hejrati and J. Mattila, "Nonlinear subsystem-based adaptive impedance control of physical human-robot-environment interaction in contact-rich tasks," *IEEE Robotics and Automation Letters*, vol. 8, no. 10, pp. 6083–6090, 2023.
- [22] A. Yeşildirek and F. L. Lewis, "Feedback linearization using neural networks," *Automatica*, vol. 31, no. 11, pp. 1659–1664, 1995.
- [23] Q. Zhang, K. Lambeth, Z. Sun, A. Dodson, X. Bao, and N. Sharma, "Evaluation of a fused sonomyography and electromyography-based control on a cable-driven ankle exoskeleton," *IEEE Transactions on Robotics*, 2023.
- [24] Y.-J. Liu, Q. Zeng, L. Liu, and S. Tong, "An adaptive neural network controller for active suspension systems with hydraulic actuator," *IEEE Transactions on Systems, Man, and Cybernetics: Systems*, vol. 50, no. 12, pp. 5351–5360, 2018.
- [25] N. Sünderhauf, O. Brock, W. Scheirer, R. Hadsell, D. Fox, J. Leitner, B. Upcroft, P. Abbeel, W. Burgard, M. Milford *et al.*, "The limits and potentials of deep learning for robotics," *The international journal of robotics research*, vol. 37, no. 4–5, pp. 405–420, 2018.
- [26] G. Tao and P. V. Kokotovic, "Continuous-time adaptive control of systems with unknown backlash," *IEEE Transactions on Automatic Control*, vol. 40, no. 6, pp. 1083–1087, 1995.
- [27] D. Recker, P. Kokotovic, D. Rhode, and J. Winkelman, "Adaptive nonlinear control of systems containing a deadzone," in *[1991] Proceedings of the 30th IEEE Conference on Decision and Control*. IEEE, 1991, pp. 2111–2115.
- [28] Z. Zhao, W. He, F. Zhang, C. Wang, and K.-S. Hong, "Deterministic learning from adaptive neural network control for a 2-dof helicopter system with unknown backlash and model uncertainty," *IEEE Transactions on Industrial Electronics*, vol. 70, no. 9, pp. 9379–9389, 2022.
- [29] X. Zhao, Z. Liu, and Q. Zhu, "Neural network-based adaptive controller design for robotic manipulator subject to varying loads and unknown dead-zone," *Neurocomputing*, vol. 546, p. 126293, 2023.
- [30] L. Li, Z. Lin, Y. Jiang, C. Yu, and J. Yao, "Valve deadzone/backlash compensation for lifting motion control of hydraulic manipulators," *Machines*, vol. 9, no. 3, p. 57, 2021.
- [31] S. Lampinen, J. Koivumäki, J. Mattila, and J. Niemi, "Model-based control of a pressure-compensated directional valve with significant dead-zone," in *Fluid Power Systems Technology*, vol. 59339. American Society of Mechanical Engineers, 2019, p. V001T01A028.
- [32] S. Kang, R. Nagamune, and H. Yan, "Almost disturbance decoupling force control for the electro-hydraulic load simulator with mechanical backlash," *Mechanical Systems and Signal Processing*, vol. 135, p. 106400, 2020.
- [33] P. Mustalahti and J. Mattila, "Nonlinear model-based controller design for a hydraulic rack and pinion gear actuator," in *Fluid Power Systems Technology*, vol. 51968. American Society of Mechanical Engineers, 2018, p. V001T01A020.
- [34] P. Mustalahti and J. Mattila, "Nonlinear model-based control design for a hydraulically actuated spherical wrist," in *Fluid Power Systems Technology*, vol. 59339. American Society of Mechanical Engineers, 2019, p. V001T01A027.
- [35] M. d. C. R. Liñán and W. P. Heath, "Controller structure for plants with combined saturation and deadzone/backlash," in *2012 IEEE International Conference on Control Applications*. IEEE, 2012, pp. 1394–1399.
- [36] M. Hejrati and J. Mattila, "Decentralized nonlinear control of redundant upper limb exoskeleton with natural adaptation law," in *2022 IEEE-RAS 21st International Conference on Humanoid Robots (Humanoids)*. IEEE, 2022, pp. 269–276.
- [37] M. Chen, S. S. Ge, and B. V. E. How, "Robust adaptive neural network control for a class of uncertain mimo nonlinear systems with input nonlinearities," *IEEE Transactions on Neural Networks*, vol. 21, no. 5, pp. 796–812, 2010.
- [38] T. Lee, J. Kwon, and F. C. Park, "A natural adaptive control law for robot manipulators," in *2018 IEEE/RSJ International Conference on Intelligent Robots and Systems (IROS)*. IEEE, 2018, pp. 1–9.
- [39] A. Harrison and D. Stoten, "Generalized finite difference methods for optimal estimation of derivatives in real-time control problems," *Proceedings of the institution of mechanical engineers, part 1: journal of systems and control engineering*, vol. 209, no. 2, pp. 67–78, 1995.
- [40] R. N. Jazar, *Theory of Applied Robotics: Kinematics, Dynamics, and Control*. Springer, 2010.